Geochemistry, Geophysics, Geosystems

RESEARCH ARTICLE
10.1029/2019GC008218

Evolution of Fine-Scale Segmentation at Intermediate-Spreading Rate Ridges

M. Le Saout[1,2], D.A. Clague[1], and J.B. Paduan[1]

[1]Monterey Bay Aquarium Research Institute, Moss Landing, California, USA, [2]Now at Geomar Helmholtz Centre for Ocean Research, Kiel, Germany

Key Points:
- Intermediate-spreading rate Alarcón Rise and Endeavour Segment illustrate past and current fine-scale segmentation
- Third-order segmentation evolves faster throughout the high magmatic phase than through the tectonic phase during which it remains steady
- Third- and fourth-order segmentation have similar characteristics along intermediate- and fast-spreading ridges

Supporting Information:
- Supporting Information S1

Correspondence to:
M. Le Saout,
mlesaout@geomar.de

Citation:
Le Saout, M., Clague, D. A., & Paduan, J. B. (2019). Evolution of fine-scale segmentation at intermediate-spreading rate ridges. *Geochemistry, Geophysics, Geosystems*, *20*. https://doi.org/10.1029/2019GC008218

Received 24 JAN 2019
Accepted 26 JUN 2019
Accepted article online 3 JUL 2019

Abstract Mid-ocean ridge axes are marked by segmentation of the axes and underlying magmatic systems. Fine-scale segmentation has mainly been studied along fast-spreading ridges. Here we offer insight into the third- and fourth-order segmentation of intermediate-spreading ridges and their temporal evolution. The Alarcón Rise and the Endeavour Segment have similar spreading rates (49 and 52.5 mm/year, respectively) but contrasting morphologies that vary from an axial high with a relatively narrow axial summit trough to an axial valley. One-meter resolution bathymetry acquired by autonomous underwater vehicles, lava geochemistry, and ages from sediment cores is combined with available seismic reflection profiles to analyze variations in (1) geometry and orientation of the axial summit trough or valley, (2) seafloor depth near the axis, and (3) distribution of hydrothermal vents, (4) lava chemistry, and (5) flow ages between contiguous axes. Along both intermediate-spreading segments, third- and fourth-order discontinuities and associated segments are similar in dimension to what has been observed along fast-spreading ridges. The Alarcón Rise and the Endeavour Segment also allow the study of the evolution of fine-scale segmentation over periods of 300 to 4,000 years. Comparison between old and young axes reveals that the evolution of fine-scale segmentation depends on the intensity of the magmatic activity. High magmatic periods are associated with rapid evolution of third-order segments, while low magmatic activity periods, dominated by tectonic deformation and/or hydrothermal activity, are associated with little to no change in segmentation.

Plain Language Summary Structure and morphology of two intermediate-rate spreading ridge axes were analyzed in 1-m resolution bathymetry collected using autonomous underwater vehicles. The observations are combined with information on the distribution of hydrothermal vents, lava flow ages, and geochemistry, and, where available, the geometry of the magma lens. The aim is to determine the third- and fourth-order segmentation of the volcanic axis along intermediate-spreading ridges and their evolution related to cycles in magma supply. The study focuses on two ridge segments, the Alarcón Rise and the Endeavour Segment, that have similar spreading rates but are in magmatic and tectonic phases, respectively, which has resulted in contrasting morphology. Our analysis shows that along both segments the third- and fourth-order segments and their associated discontinuities are similar in geometry to those observed along fast-spreading ridges, independent of the magmatic activity. However, the intensity of magmatic activity impacts the evolution of segmentation with segments that remain at the same position during tectonic or low magmatic periods and propagate, decrease, or disappear during high magmatic periods.

1. Introduction

Mid-ocean ridges display a large range of morphological, geophysical, and geochemical changes that mark discontinuities in the ridge axis and underlying magmatic system. Those discontinuities define respectively tectonic and magmatic segmentation (e.g., Carbotte et al., 2015). Macdonald et al. (1988) first proposed a classification of tectonic segmentation consisting of four different orders, from the largest discontinuities (transform faults) classified as first-order discontinuities to the smallest offsets (devals or variations in axis orientation) classified as fourth-order discontinuities. Numerous studies especially at fast- (e.g., Carbotte et al., 2000, 2004, 2013; Haymon & White, 2004; Lonsdale, 1994; Le Saout et al., 2014; Macdonald et al., 1992; White et al., 2000, 2002) and slow-spreading ridges (e.g., Gente et al., 1995; Sempéré et al., 1990, 1993) have characterized, at various scales, the different orders of segments and discontinuities. During the last two decades, high-resolution studies have improved understanding of fine-scale, third- and fourth-order ridge segmentation. At fast-spreading rate segments of the East Pacific Rise (EPR) between

27 and 32°S (Hey et al., 2004), between 8 and 12°N (e.g., Carbotte et al., 2013; Soule et al., 2009; White et al., 2006), and at 16°N (Le Saout et al., 2014), and along the intermediate-spreading rate Galápagos Spreading Center (GSC; Sinton et al., 2003), studies relating magmatic and hydrothermal processes to deep structure support a strong correlation between morpho-tectonic segmentation and magmatic lens segmentation (Carbotte et al., 2013, 2015; Marjanović et al., 2018; White et al., 2000). Tomography studies have also shown that tectonic discontinuities are associated with a decrease of mantle melt extraction, and thus, third-order segmentation of ridges has been attributed to mantle processes (e.g., Toomey et al., 2007; VanderBeek et al., 2016).

Along fast-spreading ridges, the third-order discontinuities often correspond to 0.2- to 3-km lateral offsets, with deepening of near-axis seafloor by 30-100 m, transition in eruptive fissure zone, and abrupt transition of the axial zone morphology, or changes in axis trend greater than 5°. Fourth-order discontinuities correspond to lateral offsets less than 200 m, and deepening of the near axis seafloor of 0 to 50 m (e.g., Carbotte et al., 2015; Macdonald, 2001; Macdonald et al., 1988; White et al., 2000, 2002). At the intermediate-spreading rate GSC and the South Eastern Indian Ridge, segmentation associated with variation of surface morphology such as changes in ridge trend greater than 5°, abrupt transition of the axial zone morphology, small lateral offsets (<2 km), or transitions in eruptive fissure zone have been described (e.g., Carbotte et al., 2015; Christie et al., 2005; Sinton et al., 2003; White et al., 2008). However, due to a lack of high-resolution data, previous studies on fine-scale segmentation along intermediate-spreading ridges have been unable to distinguish between third- and fourth-order segmentation (Carbotte et al., 2015).

It is also uncertain how segmentation evolves through time. The rugged morphology of intermediate-spreading ridges, which often have deep rift valleys and domed axial highs, reflects variations in tectono-magmatic balance (Buck & Poliakov, 1998; Carbotte et al., 2006; Kappel & Ryan, 1986; Lewis, 1979; Malinverno & Pockalny, 1990; Pezard et al., 1992; Poliakov & Buck, 1998; Clague et al., 2014). Fine-scale segmentation along intermediate-spreading ridges has only been examined previously on segments with an axial high, and the evolution of fine-scale segmentation within a tectono-magmatic cycle has not been studied. Third- and fourth-order discontinuities rarely leave recognizable off-axis traces (Macdonald et al., 1992; White et al., 2000). These processes can only be investigated along the neo-volcanic zone using high-resolution bathymetry.

The Alarcón Rise and the Endeavour Segment offer an opportunity to analyze fine-scale segmentation at intermediate-spreading ridges and address these questions. First, they are mapped partially (Endeavour Segment) or entirely (Alarcón Rise) by 1-m bathymetric data (Clague et al., 2014, 2018). They have similar spreading rates but contrasting morphology, with an axial high at the Alarcón Rise and an axial valley (AV) at the Endeavour Segment, that allows comparison between different phases of the tectono-magmatic cycle. In addition, both segments display past and current segmentation allowing us to evaluate how the accretionary behavior at intermediate-spreading ridges evolves during high and low magmatic periods.

2. Geological Setting

2.1. Alarcón Rise

The Alarcón Rise, located between 23°13′N and 23°39′N in the mouth of the Gulf of California, is the northernmost segment of the EPR (Figure 1a). Its full spreading rate is estimated at 49 mm/year (DeMets et al., 2010). This 50-km-long segment is a first-order tectonic unit bounded by the transtensional Tamayo Transform Fault to the south and the Pescadero Transform Fault to the north (Figure 1b; Clague et al., 2018). The Alarcón Rise has a rifted axial high characterized by a relatively narrow axial summit trough. Its depth varies from 2,700 to 2,230 m below sea level and its width from 2.2 to 5.9 km. The segment is more inflated and shallower in its southern half, between 23°20′N and 23°23′N, where magmatic activity is thought to be highest (Clague et al., 2018). Along the ridge, 109 hydrothermal chimneys have been identified through seafloor mapping and remotely operated vehicle observations (Paduan et al., 2018). At least 31 chimneys are active and distributed in four high-temperature hydrothermal vent fields (Figures 2a and 2d; Caress et al., 2015; Paduan et al., 2018).

The Alarcon Rise is a relatively recent ridge that initiated about 2-3 Ma ago (Lizarralde et al., 2007; Sutherland, 2006). On both side of the axis the alternation of parallel ridge crests and relatively

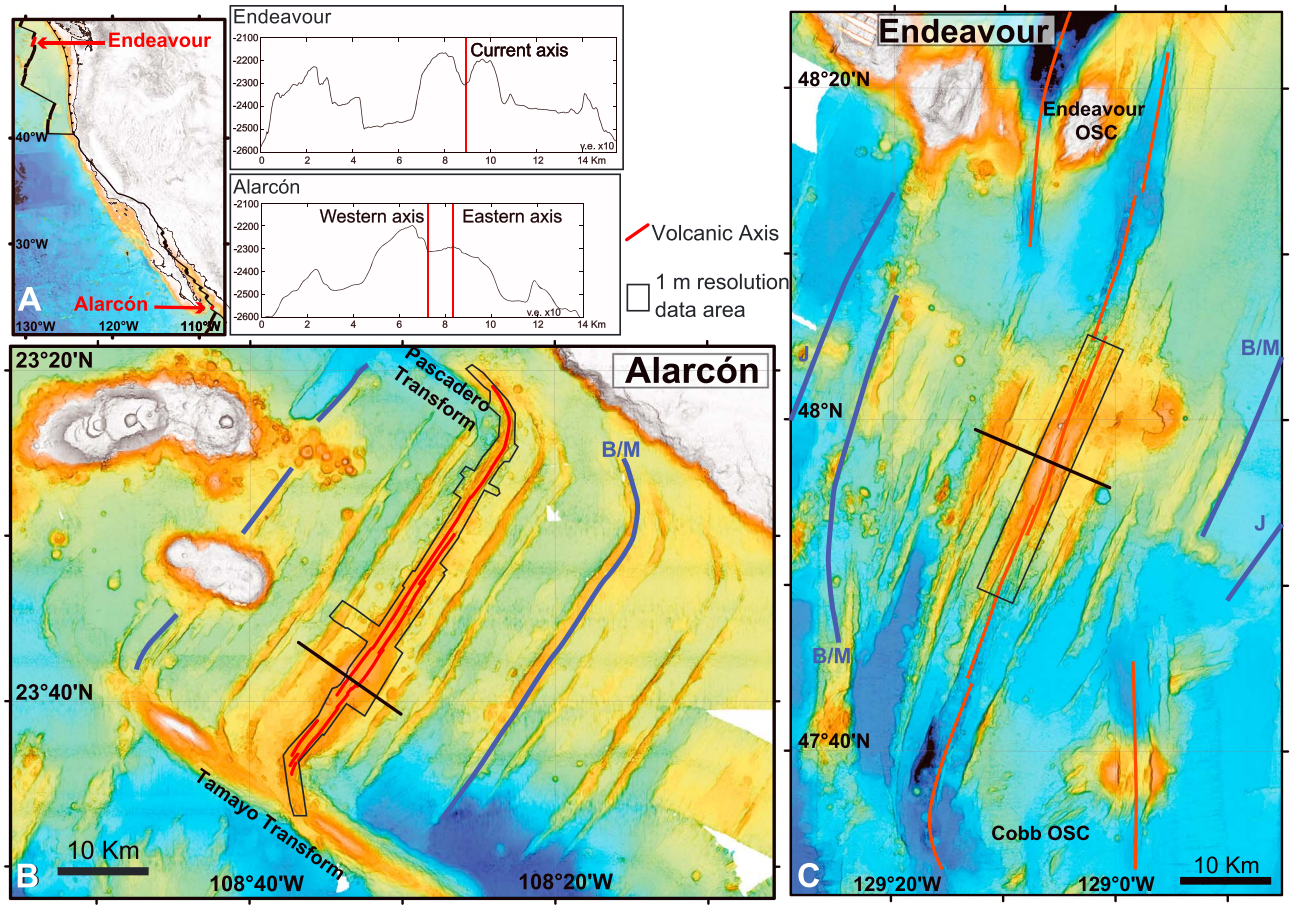

Figure 1. (a) Map of the northeast Pacific Ocean, showing tectonics of the region and the study areas in red. (b) Regional bathymetric map of the Alarcón Rise bounded by the Tamayo and Pescadero Transforms. (c) Regional bathymetric map of the Endeavour Segment bounded by Endeavour and Cobb overlapping spreading centers. The Endeavour Segment and the Alarcón Rise maps show the volcanic axes (red) and the coverage of the *autonomous underwater vehicles* bathymetry (black box). Profiles 1 and 2, across the axes of the two segments, are indicated by black lines, and the Brunhes/Matuyama (B/M) and Jaramilo (J) magnetic isochrons are indicated by blue lines (Lonsdale, 1994).

flat-floored graben have been interpreted as the result of the variation between magmatic and tectonic phases as modeled by Kappel and Ryan (1986). The morphology of the axis and the flow ages indicate that the Alarcón Rise is currently in a magmatic phase that has lasted more than 10,000 years, based on ages of lava flows inferred from ^{14}C dating of planktic foraminifera at the base of sediment cores (Clague et al., 2018). The presence and geometry of a magma lens are unknown due to the lack of multichannel seismic data.

2.2. Endeavour Segment

The Endeavour Segment, located between 47°35′N and 48°13′N, is one of the seven second-order segments of the Juan de Fuca Ridge (Figure 1a). It has a full spreading rate estimated at 52 mm/year (DeMets et al., 2010), only 3 mm/year greater than the rate of the Alarcón Rise. This-90-km-long segment is bounded by the Endeavour Segment overlapping spreading center (OSC) to the north and by the Cobb OSC to the south (Figure 1c; e.g., Cousens et al., 1995; Karsten et al., 1986, 1990; Van Ark et al., 2007). The Endeavour Segment has a 0.8- to 1.7-km-wide and 100- to 200-m-deep AV (Clague et al., 2014; Delaney et al., 1992, 1997; Glickson et al., 2007). The valley is wider at its distal ends and narrow toward its center where the AV is bounded by the previous axial high (25 km long, 4 km wide, and 300 m high) located between 47°54′N and 48°3′N (Van Ark et al., 2007). This region marks the shallowest portion of the ridge axis with the valley floor reaching 2,131 m in depth. The central portion of the ridge also hosts all known hydrothermal activity on the segment. Five major active fields were discovered via submersible observations and sampling, water column thermal

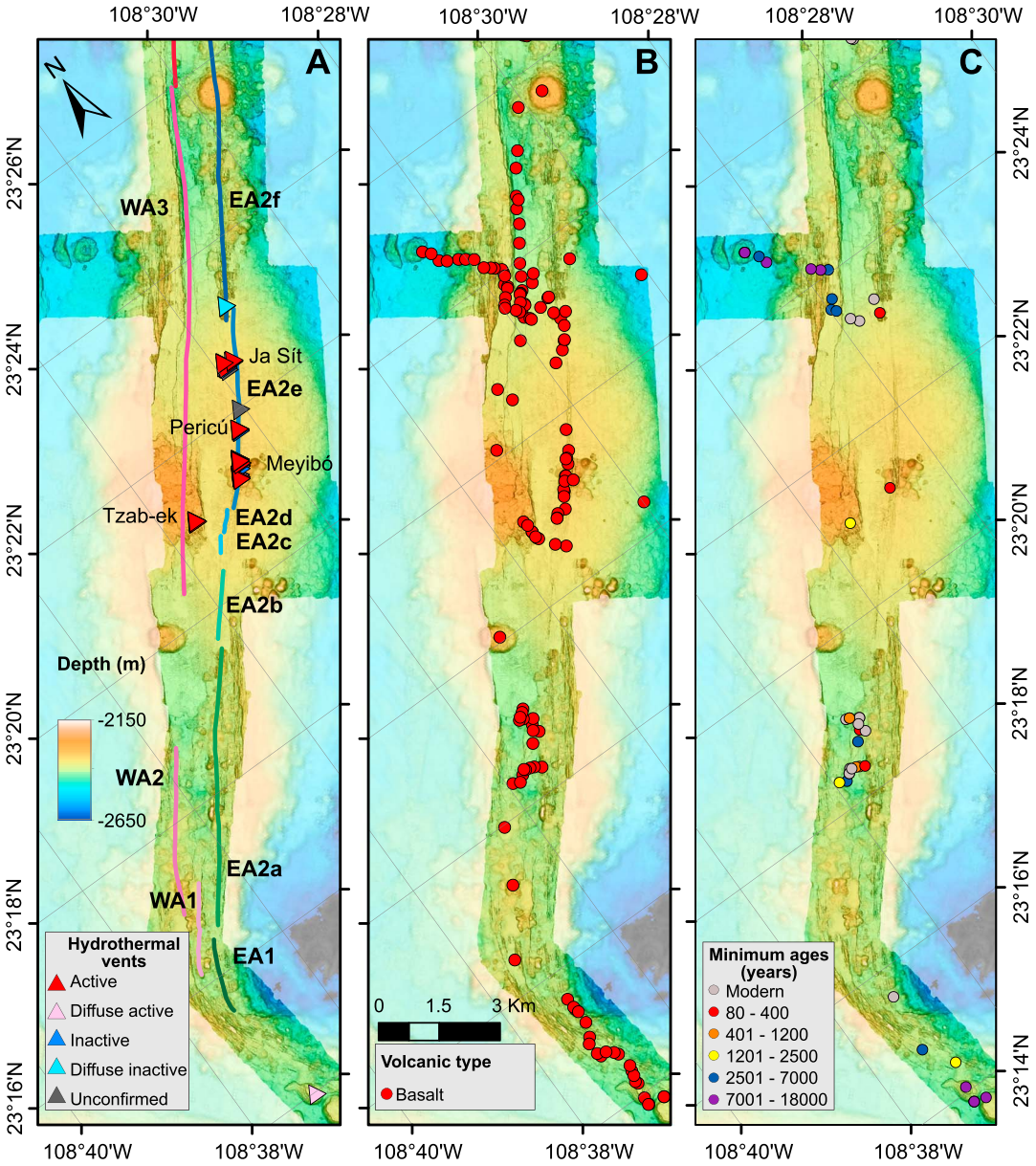

Figure 2. Maps showing the Alarcón Rise segment volcanic axes, lava composition and flow ages on autonomous underwater vehicles bathymetry gridded at 1 m resolution superimposed on faded ship-based multibeam bathymetry. (a-c) Southern half of the Alarcón Rise; (d-f) northern half of the Alarcón Rise. (a and d) The center of each volcanic axis is indicated by a colored bold line. Third- and fourth-order segment names are indicated near each axis. The hydrothermal chimneys are indicated by triangles, and their activity is indicated using a color code (Paduan et al., 2018). The four active vent fields are named. The location of Figure 4 is indicated by a red box. (b and e) Maps of the distribution of the lava samples from remotely operated vehicle dives colored by rock type from basalt to rhyolite (Clague et al., 2018). (c and f) Maps of the distribution of the sediment cores collected during remotely operated vehicle dives colored by radiocarbon ages of the basal section (Clague et al., 2018).

and chemical anomalies and dredging. They are named Sasquatch, Salty Dawg, High Rise, Main Endeavour, and Mothra from north to south (e.g., Bhat et al., 1997; Delaney et al., 1992; Kelley et al., 2001; Lilley et al., 1995; Robigou et al., 1993; Tivey & Delaney, 1986; Van Ark et al., 2007) and include current high-temperature (300-400°C) activity. More recent studies based on high-resolution seafloor mapping have identified 581 chimney structures in the area, most of them concentrated in, but not limited to, the five major vent fields (Clague et al., 2014; Jamieson et al., 2014).

Over the past several millions of years, the Endeavour Segment has experienced different episodes of non-steady-state regression and propagation that has resulted in several readjustments of the Cobb OSC

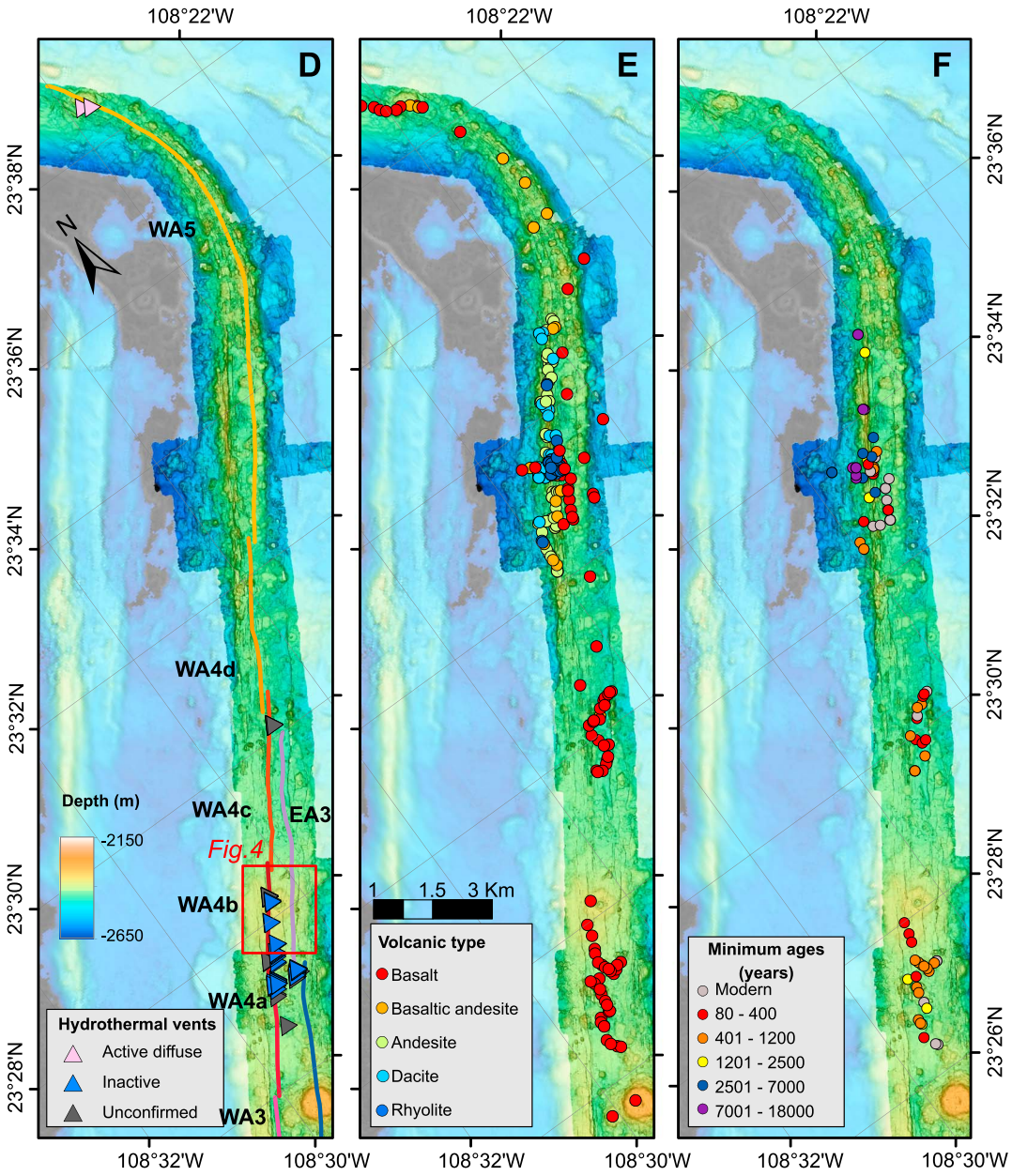

Figure 2. *(continued)*

location (Shoberg et al., 1991; Wilson, 1993). As with the Alarcón Rise, the Endeavour Segment also experienced variations in accretion processes, reflected by the alternation of ridge crests and valleys parallel to the ridge axis. Clague et al. (2014) inferred lava flow minimum ages from the ^{14}C dating of planktic foraminifera at the base of sediment cores (Clague et al., 2014) and used ages of overlying sulfide samples (Jamieson et al., 2013). They proposed that during the last 10,000 years, the segment has gone through three different phases: magmatic, tectonic, and hydrothermal. This current phase consists of intense hydrothermal activity with low volcanic output and high tectonic activity (Clague et al., 2014). Even though characterized by low volcanic activity, multichannel seismic data reveal that a discontinuous magma lens underlies the central and shallowest 20 km of the ridge. The magma lens is 0.5-1.2 km wide and located 2.1 to 3.3 km below the seafloor (Van Ark et al., 2007). Using variations in the depth and amplitude of the reflector, Van Ark et al. (2007) identified three disruptions of the magma lens at ~47°54.7′N, 47°56.8′N and 48°0.5′N.

3. Data, Terminology, and Methods

3.1. Data

This study uses 1-m horizontal resolution bathymetry collected by autonomous underwater vehicles (AUV), here referred to as AUV bathymetry. At the Alarcón Rise, the axial high is fully mapped over a distance of 51.5 km, from transform fault to transform fault (from 23°13′N to 23°39′N) with 1-m-scale coverage of ~164 km^2 (Figure 1b). The data were collected in 2012 and 2015 using the MBARI AUV *D. Allan B.* equipped with a Reson 7125 200-kHz multibeam sonar (Clague et al., 2018). Along the Endeavour Segment, the 1-m-scale bathymetry covers a length of 23 km between 47°52.5′N and 48°4.6′N (Figure 1c; Clague et al., 2014) and was acquired in 2008 and 2011 using the same AUV *D. Allan B.* (Clague et al., 2014). The final grid also includes bathymetry acquired in 2005 using the AUV *ABE* equipped with a Simrad Mesotech SM2000 multibeam sonar (Glickson et al., 2007; Kelley et al., 2012).

3.2. Terminology

In this paper, we consider the *volcanic axis* (VA) as the locus of magmatic activity when the ridge has an axial high (e.g., Alarcón Rise), whether the VA is expressed on the seafloor as a single fissure, a swarm of fissures, a graben, or by a volcanic ridge. Eruptive fissures, hybrid fractures, and grabens are as illustrated in Figure 3 of Le Saout et al. (2018). In the case of the Endeavour Segment, which is characterized by an AV, a narrow VA is not well defined. We thus considered the geometric variability of the AV and used its center as the center of the magmatic/tectonic activity. Finally, lava flows are described based on their flow-scale morphology as used by Clague et al. (2017, 2018) instead of lava morphology. We use the term "channelized flows" to describe lobate flows with sheet flow channels and pillow margins and "hummocky flows" to describe mounds or coalesced mounds that mainly consist of pillow lava.

3.3. Methods

The analyses of AUV bathymetric data collected along the two segments allow us to identify volcanic axes and infer where previous axes had been, by using the obvious fissure system in the young sheet flow, the axes of fracture swarms that appear to be the center of extrusion, or the axes of pillow ridges. Cross sections perpendicular to the axes were drawn as in the examples shown in Figure 1. These transverse profiles were drawn every 100 m along axis and extended 2,400 m across for the Endeavour Segment and 1,200 m across for the Alarcón Rise. In total, 343 profiles were analyzed for the Endeavour Segment and 865 for the Alarcón Rise. On each profile, we have systematically identified (1) the top and the bottom of the eastern and western rim of the graben or AV (Figure S1a in the supporting information), (2) the top of the eastern and western limit and the bottom of the fissure (Figure S1b), or (3) the summit of volcanic ridges when no fissures were observed (Figure S1c). Thus, for each profile, the across-axis widths of the VA and AV, and the mean depths of the axis, near-axis sea floor, and AV were measured. These were compiled to determine cross-axis and along-axis variations of the geometry of the ridge. Deformation was evaluated from fracture patterns, and horizontal extension across axes was calculated by summing the horizontal displacement associated with the fractures, as described in Le Saout et al. (2018); Figure S2).

4. Observations

4.1. Alarcón Rise

The Alarcón Rise has two parallel volcanic axes that overlap for a distance of about 31 km from 23°16′N to 23°30′N (Figures 2a and 2d). These two axes are 85 to 1,300 m apart with a maximum distance reached near 23°21.85′N, where the axial ridge is the most inflated. We refer to these axes as eastern axis (EA) and western axis (WA). The EA is the source of the youngest flow on the Rise (Clague et al., 2018) and slowly disappears to the north. North of 23°30′N the EA is not resolved and the VA is described as part of the WA (Figure 2d).

4.1.1. Morphology of the Alarcón Rise Axes

The eastern VA is disrupted by two 320- to 465-m wide lateral offsets (Table 1) that define three 1.4- to 23.5-km-long third-order segments named EA1 to EA3 (Figure 2a and Table 2). These discontinuities coincide with deepening of the seafloor along the axis of 75 and 100 m (Figure 3c and Table 1) and with variation of the axis trend up to 15° (Table 1). Within the third-order segment EA2, five smaller disruptions are associated with 87- to 210-m lateral offsets (Table 1). These discontinuities subdivide EA2 into six 0.4- to 9.1-km-long fourth-order segments named EA2a to EA2f (Figure 2a and Table 2). No clear variation of

Table 1
Characteristics of the Fine-Scale Discontinuities Along the Endeavour Segment and the Alarcón Rise

Latitude	Discontinuity order	Seefloor deepening (m)	AV/VA lateral offset[a] (m)	AV/VA variation[b] (m)	AV/VA trend variation (°)	change in volcanic facies	Change in composition	change in hydrothermal distribution	Magma lens disruption[c]
Alarcón Eastern axis									
23°16.4′N	Third	75	465	yes	15	?	no	no	NO seismic data
23°19.56′N	Fourth	no	105	yes	3	yes	no	no	
23°20.3′N	Fourth	no	96	no	4	no	no	no	
23°20.6′N	Fourth	no	87	no	5	no	no	no	
23°20.9′N	Fourth	no	210	no	5	no	no	yes	
23°23′N	Fourth	no	148	yes	2	yes	no	yes	
23°27.2′N	Third	100	320	yes	4	no	no	yes	
Alarcón Western axis									
23°16.5′N	Third	50	550	yes	2	no	no	no	NO seismic data
23°19.5′N	Third	75	?	yes	4	no	no	yes	
23°26′N	Third	120	90	yes	6	no	no	yes	
23°27.2′N	Fourth	no	149	yes	2	no	no	no	
23°28.7′N	Fourth	no	137	yes	0	no	no	yes	
23°30.4′N	Fourth	no	178	no	3	no	no	yes	
23°32.3′N	Third	90	170	yes	2	yes	yes	yes	
Endeavour Segment									
47°55.56′N	Third	Not evidenced	565	>250 m	2	Not evidenced	Not evidenced	yes	47°54.7′N
47°58.6′N	Fourth?		510	no	3			yes	no
48°1.2′N	Third		946	>200 m	1			yes	48°00.5′N

Abbreviations: AV, axial valley; VA, volcanic axis.
[a]Lateral distance between two contiguous axial valley (AV) or volcanic axis (VA). [b]Change in depth and/or width between two axial valley or volcanic axis.
[c]Interpreted based on seismic reflection profiles (Van Ark et al., 2007).

Table 2
Morphological Characteristics of the Endeavour Segment and the Alarcón Rise Third- and Fourth-Order Segments[a]

Axis[a]	Length (km)	Depth (m)	Width (m)	Young flow area (km^2)	Flow ages (year BP)	Hydrothermal vents	Vents field
Alarcón Rise							
EA1	1.4	3.5-16.5	20-179	Not determined	no data	no	Meyibo, Ja sit, Pericu
EA2	23.5						
a	6.6	0.5-17.6	1-325		Modern-169	no	
b	1.9	1-7.6	15-78		no data	no	
c	0.4	0.6-8.7	6-27		no data	no	
d	0.4	0.8-2.3	6-18.7		no data	no	
e	4.9	0.5-16.2	3-167		Modern - 295	active	
f	9.1	0.5-22	5-371		Modern	inactive	
EA3	6.3	0.5-9.5	1-429		89-350	no	
WA1	1.5	4-14.5	6.5-39		no data	no	
WA2	4.6	volcanic ridge			2110	active	Tzab-ek
WA3	11.3	5-33.9	190-564		> 1145	no	
WA4	14				89-2222		
a	3.9	0-6.8	0-64.4		89-1173	inactive	
b	2.7	0.5-9.2	94-389		no data	inactive	
c	4.1	0-16	0-236		no data	inactive	
d	4.3	0-17	0-195		280-2222	no	
WA5	13.9	1-22.8	3-256		Modern-11750	active	
Endeavour Segment							
AV1	> 5.7	22.2-116.2	192.5-834.5	0	no data	active & inactive	
AV2	14.7			0.74			
a	14.5	12-99.6	234.5-1340.5	0.63	101-9314	active & inactive	MEF, HR, M
b	7.2	12.9-57.8	186.5-617	0.11	Modern-1554	active & inactive	S, SD
AV3	> 6.9	27-105.5	240-832	0	no data	no detected	

[a]Depth and width are measured based on bathymetric cross sections, 1,200 m long and 100 m for the Alarcón Rise and 2,400 m long and 100 m apart for the Endeavour Segment. Ages are inferred from ^{14}C dating of the basal section from sediment push cores (Clague et al., 2014, 2018) and from sulfide samples (Jamieson, 2013). The Endeavour vent fields are indicated by their abbreviation: Main Endeavour Field (MEF), High Rise (HR), Mothra (M), Sasquatch (S), and Salty Dawg (SD).

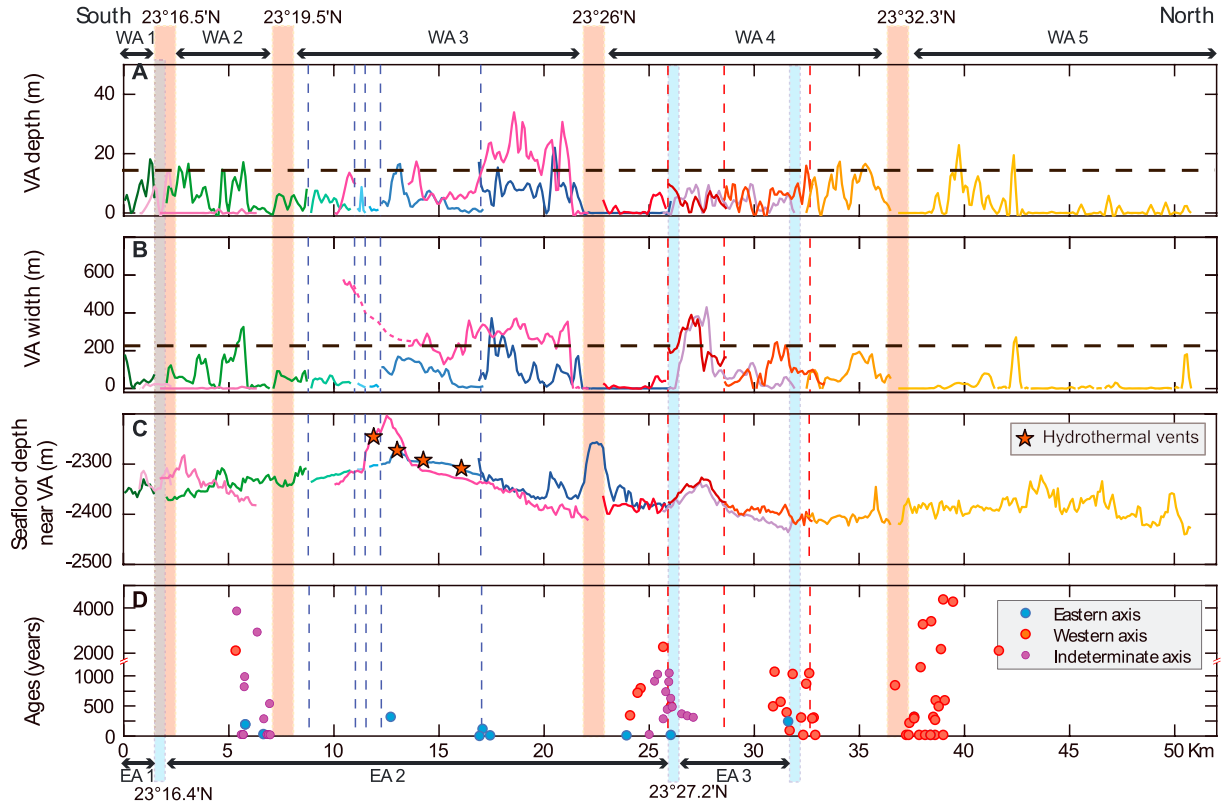

Figure 3. Along-axis variations of the volcanic axis (VA) morphologies of the Alarcón Rise. The eastern axes are colored from green to purple, the western axis from red to yellow. Third-order discontinuities are indicated by wide vertical lines (light blue for eastern discontinuities and light red for western discontinuities) and fourth-order discontinuities apparent in the bathymetry by vertical dashed lines. (a) Variations of volcanic axis depth measured based on cross-sections perpendicular to the axis. (b) Variations of the volcanic axis width. (c) Variations of the seafloor depth in the vicinity of the volcanic axis, measured on transverse bathymetric cross-sections. The main hydrothermal vents are located by orange stars. (d) ^{14}C ages from the basal section of sediment cores used to estimate minimum ages of the underlying flows (Clague et al., 2018). The ages are distributed depending on their location along the eastern (blue) or western axis (red). Samples with an indeterminate axis of origin are in purple.

the seafloor depth near the axis is observed at these discontinuities, and variation of the axis trend remains smaller than 5°. Independent of the order of the discontinuity, the morphology of the axis varies between the different segments. EA1 and EA2b to EA2e are defined by a single eruptive fissure, while the other segments are defined by a swarm of fissures (EA2a and 2f) or a graben (EA3). These volcanic axes also display significant variability in depth and width (Figure 3 and Table 2). Their depth is from 0.5 to 22 m shallower than the adjacent floor but is generally less than 15 m (Figure 3a). Their width ranges from 1 to 429 m but is generally less than 200 m (Figure 3b).

Along the western VA, the discontinuities are often less obvious as the transition between the different segments is usually partially or totally erased by flows erupted along EA. However, four large discontinuities are identified defining five 1.5- to 14-km third-order segments named WA1 to WA5 (Tables 1 and 2). Except at 23°16.5′N (between overlapping WA1 and WA2), where the lateral offset is 550 m, the other discontinuities have lateral offsets less than 200 m. All discontinuities are associated with a change in the axis trend less than 6° (Table 1). As along the EA, these third-order discontinuities coincide with deepening of the seafloor near the axis of 50-120 m compared to each segment center. WA4 is the only third-order segment clearly disrupted by smaller discontinuities associated with 137- to 178-m lateral offsets but that do not coincide with seafloor deepening (Table 1). Those discontinuities subdivide WA4 into four fourth-order segments named WA4a to WA4d (Figure 2d). All these discontinuities mark variations in depth and width of the VA. WA2 and WA5 consist primarily of a volcanic ridge with a relative absence of eruptive fissures or graben that usually define the segment axis. WA1 appears to have been modified by younger deformation that contributed to the asymmetric growth of the axis with the development of the eastward-facing scarp that reached 15

m in height. WA3 and WA4b consist of a wide graben (up to 600 m in width and 34 m in depth; Figure 3 and Table 2). WA4a, 4c, and 4d consist of a graben partially covered by small pillow mounds (Figure 3). The dimensions (depth, width, and length) of these volcanic axes may be underestimated. Indeed, the western wall of the graben may have been affected by more regional deformation resulting in the asymmetry of the graben, and flows erupted along EA often mask the eastern bounding fault and partially or completely fill the graben.

4.1.2. Lava Flow Morphology, Composition, and Ages

Hummocky flows dominate the entire axis, and channelized flows are mainly observed in the inflated and more magmatic part of the segment between 23°19′N and 23°24′N (Clague et al., 2018). In more detail, each VA is characterized by a main flow morphology. EA2b, 2c, 2d, and 2e are dominated by channelized flows. The WA, EA1, 2a, 2f, and 3 consist dominantly of hummock flows. Along WA1, WA2, WA4a, 4c, 4d, and WA5 the hummocky flows form volcanic ridges or cones, while WA4b and EA3 are dominated by a low shield volcano (Figure 2a).

The Alarcón Rise lavas are also characterized by a wide range of compositions from primitive mid-ocean basalt to rhyolite (Figures 2b and 2e; Clague et al., 2018). South of 23°32′N, all axes have lava flows with basaltic compositions. However, in the northern part of the ridge, the flows display a wider geochemical variability. Lava flows in WA5 are the most evolved lavas of the Alarcón Rise. At the axis, the flows consist of basalt and basaltic andesite, whereas on the western flank the lavas are andesite, dacite, and rhyolite compositions (Figures 2b and 2e; Clague et al., 2018).

^{14}C ages of basal sediment in cores were used to infer minimum ages of the underlying flows (Clague et al., 2018). Those ages vary from 80 years to 12 kyr (Figure 2c). The EA is characterized by flows younger than 350 years (Figures 2c and 3d and Table 2), with the youngest flows erupted along EA2b to EA2e, where often too little sediment had accumulated to collect cores. Flows along the WA are usually older and reach 12 kyr. Along WA5, older flows are more evolved than flows younger than 300 years, which have basaltic compositions (Clague et al., 2018).

4.1.3. Deformation

Along the Alarcón Rise, most faults and fractures occur directly along the VA indicating that most deformation probably results from dike intrusions (e.g., Carbotte et al., 2006; Chadwick & Embley, 1998; Cormier et al., 2003; Le Saout et al., 2014, 2018; Soule et al., 2009; Szitkar et al., 2016). Some off-axis fractures are also observed especially near the Tamayo transform fault, where flows are modified by fractures that are not associated with intrusion, but rather with tectonic faulting (Figure 2a). The deformation is usually different between WA and EA. WA mainly has an asymmetric graben, whereas most of the deformation along EA is expressed by a single fissure or swarm of fissures (Figure 2a). WA4b and EA3 are parallel segments with similar dimension grabens (330-375 m wide and 3-6 m deep for WA4b and 330-375 m wide and 5-10 m deep for EA3; Figure 4). They also mark the only place where an average deformation rate due to dike intrusions can be estimated. Between 23°27.5′N and 23°28.5′N, WA4b and EA3 cross a large probably monogenetic volcanic shield that predates deformation along both axes and is younger than ~320±30 years (Clague et al., 2018). The horizontal extension across both axes can be calculated by summing the horizontal displacement associated with the fractures that modified the shield. That extension is 15 to 21 m along WA4b and 24 to 46.5 m along EA3 (Figures 4b-4d). During the same period, EA3 accommodates 29 to 54% more extension than WA4b.

4.1.4. Hydrothermal Vent Distribution

All hydrothermal vents identified on the AUV bathymetry are located within or on the edge of the two volcanic axes (Figures 2a and 2c). The 31 active chimneys are distributed in four hydrothermal fields located between 15°20.5′N and 15°23′N in the inflated part of the ridge. Meyibó, Ja sít, and Pericú high-temperature hydrothermal vent fields are located along EA2e (Figure 2a and Table 2; Clague et al., 2018; Paduan et al., 2018). Tzab-ek vent field is located along WA3. Inactive chimneys are mainly located between 15°26.5′N and 15°28.5′N at the southern ends of EA3 and WA4a.

4.2. Endeavour Segment

4.2.1. Morphology of the Axis

Along the Endeavour Segment, eruptive fissures are not as evident as along the Alarcón Rise, and changes in orientation of the walls of the axial graben are used to evaluate the structure of the axis. The Endeavour

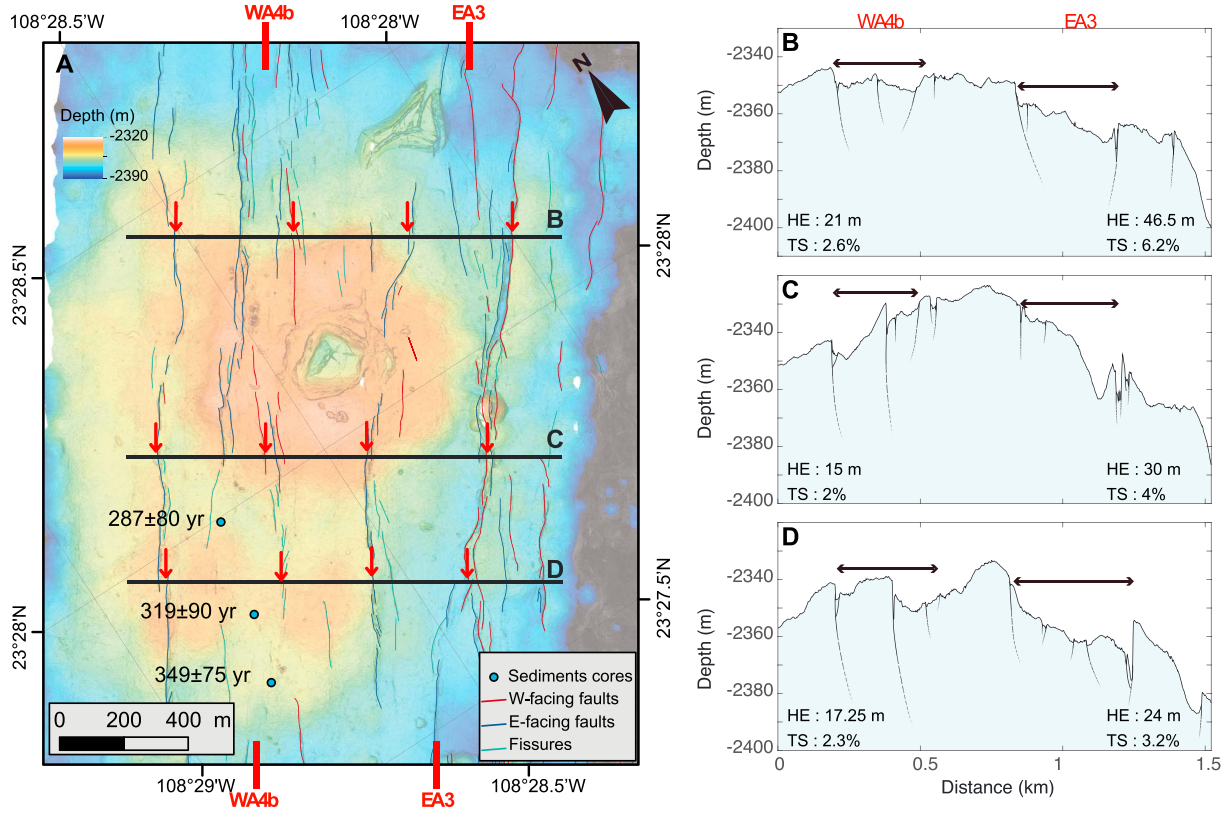

Figure 4. (a) Map of the large volcanic shield cut by EA3 and WA4b. The shield dated at 320±30 year BP (Clague et al., 2018) is used to estimate the difference in deformation along the eastern and western axes. The three cross-sections used to estimate the horizontal extension are located by bold lines. The red arrows along each cross section indicate the margins of the eastern and western grabens. (b–d) Cross-section profiles showing the fractures associated with the eastern and western axes (graben widths shown between arrows on bold lines). The horizontal extension (HE) and tectonic stress (TS) for each axis are indicated below each profile.

segment AV is disrupted by two 565- to 950-m lateral offsets of the axis between 47°53′N and 48°4.6′N (Figure 5 and Table 1). These offsets delimit three third-order segments named AV1 to AV3 from south to north (Figure 5a and Table 2). AV1 and AV3 extend beyond the mapped area, so exceed 5.7 and 6.9 km in length, respectively. AV2, the only entirely mapped segment, is 14.7 km long. The depth of all AV varies from 12 to 116 m with respect to the adjacent floor (Figure 6a). AV1 and AV3 correspond to the deeper parts of the AV. Their width varies from 190 to 1,340 m, with AV3 having the widest valley (Figure 6b). Along the three AV, both depth and width reach their maxima near the center of the AV and decrease toward the ends (Figures 6a and 6b). No clear discontinuity is observed in the seafloor depth measure at the edges of the valley (Figures S1 and 6c). However, the two discontinuities correspond to the northern and southern limit of the rifted axial high (Figure 5a).

Within AV2, no discontinuity is observed in the valley wall; however, around 47°58.6′N, a horst divides the northern part of the valley into two parallel segments offset by 510 m (Table 1). The WA, observed on the entire length of AV2, is named AV2a, while the EA, only observed north of 47°58.6′N, is named AV2b (Figures 5 and 6).

4.2.2. Lava Flow Morphology, Composition, and Ages

Lava flows in the AV are highly modified by fractures. Thus, the distinction of flow morphologies is often unclear, but the main flow morphology seems to be hummocky and no strong variations are observed among the segments. Within the valley, only 12 flows have relatively low fracture density. They are all located along AV2, where they cover a total surface area of 0.75 km^2 (Figure 5c and Table 1) and all consist of channelized flows (collapsed sheet flows). North of 47°58.6′N the younger flows are observed on both sides of the horst that delimits AV2a and AV2b.

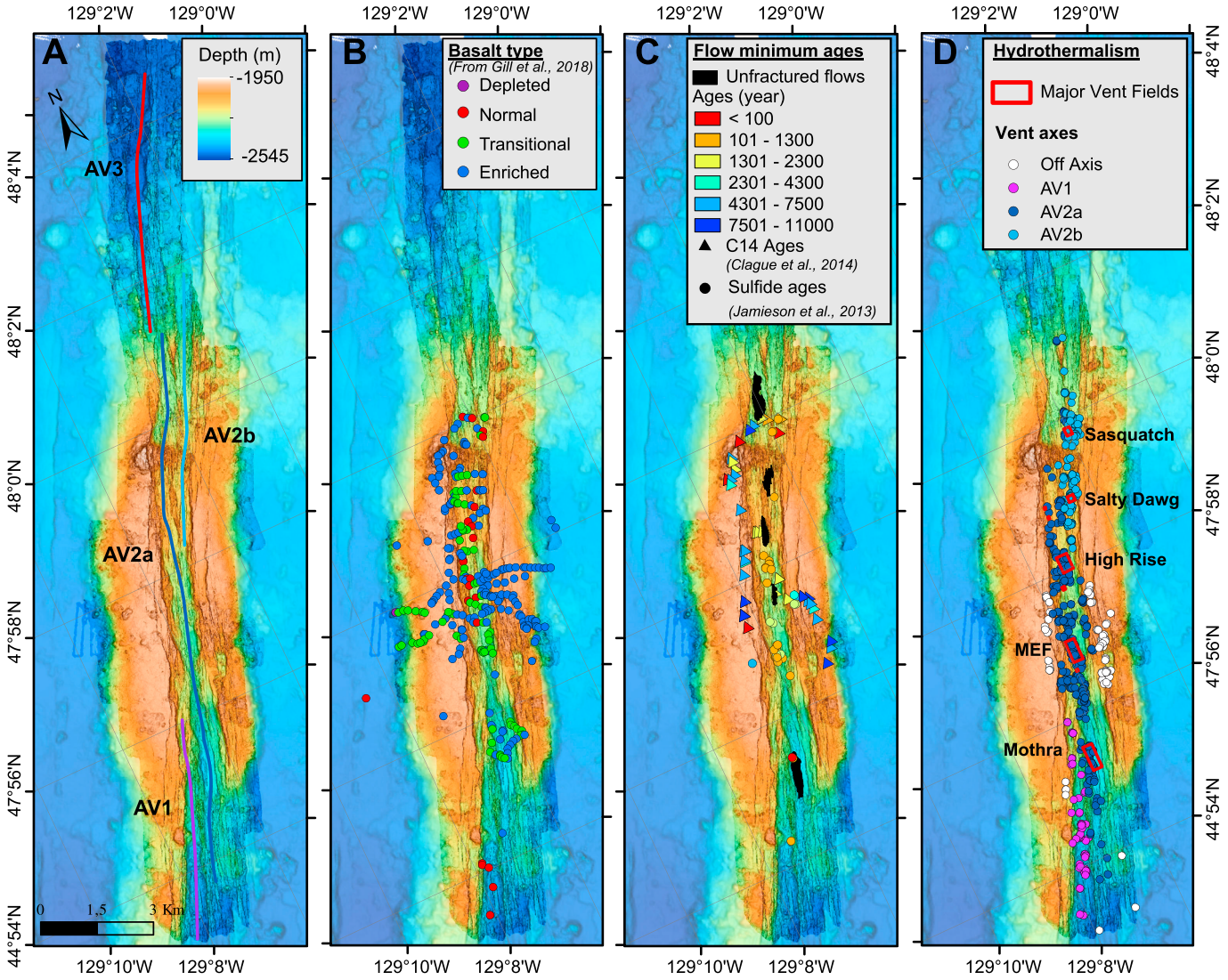

Figure 5. Autonomous underwater vehicles *D. Allan B.* Autonomous underwater vehicles bathymetry gridded at 1-m resolution of the Endeavour Segment, with *ABE* data gridded at 4 m and background Simrad EM302 shipboard (TN298) multibeam swath data gridded at 30 m. (a) The center of each axial valley named is outlined by a bold line. Third- and fourth- segment names are indicated. (b) Map of the distribution of the lava samples from remotely operated vehicle dives colored by basalt type from depleted to enriched mid-ocean ridge basalt (Gill et al., 2018). (c) Distribution of flow minimum ages determined using sulfide samples from Jamieson et al. (2013) and ^{14}C ages from the basal section of sediment cores from Clague et al. (2014; triangles and circles, respectively, subdivided using the same age color code). The five young unfractured lava flows are shown in black (from Figure 6 of Clague et al., 2014). (d) Distribution of hydrothermal chimneys within the axial graben and outside the valley (from Jamieson et al., 2014). Mothra, MEF, High Rise, Salty Dawg, and Sasquatch vent fields are enclosed by red boxes.

Lava compositions along the Endeavour Segment vary from depleted to enriched mid-ocean ridge basalt (MORB) and are distributed in seven chemically distinct basalt types (Figure 5b; Gill et al., 2016; 2018). Rock sampling was focused on the center part of the segment within and on both sides of AV2. Only five samples were collected along AV1, and no sampling was done along AV3. However, AV1 and AV2 show two distinct compositions. AV1 lavas are normal MORB composition, while AV2 lavas are primarily composed of enriched and transitional MORB with few normal MORB close to the axis (Gill et al., 2018)

Radiocarbon ages of basal sediment in cores (Clague et al., 2014) and isotopic sulfide ages (Jamieson et al., 2013) are used to infer minimum flow ages. On the flank of the AV, the minimum flow ages range from 1426 to 10,740 year BP (Table 2). Within the AV, minimum ages vary from Modern to 9,314 year BP but are mostly younger than 2,210 year BP (Figure 5c). No ages were measured along AV1 and AV3 to allow comparisons.

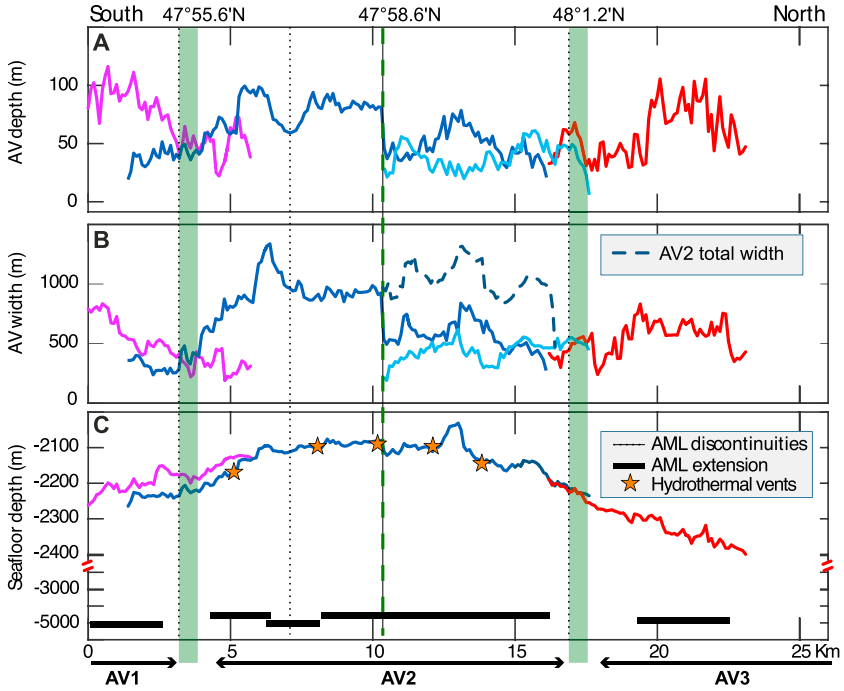

Figure 6. Along-axis variations of the axial valley (AV) of the Endeavour Segment. The axes are represented in purple for AV1, blue for AV2, and red for AV3. Third-order discontinuities are indicated by a wide vertical green line the fourth-order discontinuity by a vertical green dashed line and discontinuities of the magma lens identified on seismic reflection profiles (Van Ark et al., 2007) by vertical dotted lines. (a) Variations of axial valley depth measured on cross sections perpendicular to the axis. (b) Variations of axial valley width. (c) Variation of seafloor depth in the vicinity of the axial valley, measured on transverse bathymetric cross-sections. The main hydrothermal vents are located by orange stars. The extent along the axis of the axial magma lens (AML) is shown by black rectangles.

However, that AV2 is the only segment with unfaulted flows indicates that the most recent volcanic activity occurs along AV2.

4.2.3. Hydrothermal Vent Distribution

Hydrothermal activity along the Endeavour Segment is distributed within and on both sides of AV1 and AV2. No hydrothermal chimneys have been identified along AV3 (Figure 5d). AV2 is the most hydrothermally active part of the valley and contains 75% of the hydrothermal chimneys, including the five large active hydrothermal fields named Mothra, Main Endeavor, High Rise, Salty Dawg, and Sasquatch. The distribution of hydrothermal chimneys is offset in two locations. The first is part way along the overlapping transition between AV1 and AV2 where the hydrothermal axis is shifted by 500 m toward the east. The second offset is located within AV2 at ~47°58.6′N, where the hydrothermal axis is shifted by ~510 m toward the east (Figure 5d and Table 2). This second offset, within AV2, coincides with a subdivision of the AV.

5. Discussion

5.1. Volcanic Axis Segmentation

5.1.1. Alarcón Segmentation

At the Alarcón Rise, magmatic activity has been focused along two parallel and relatively contiguous volcanic axes, with the most recent activity along the EA (Figure 3d). Both axes are subdivided by discontinuities. The larger discontinuities are associated with lateral offsets and deepening of the seafloor greater than 300 and 50 m, respectively, and are similar to those that delimited third-order segments as defined by Macdonald et al. (1988; Table 1). Those third-order segments are themselves composed of a single segment or are broken in multiple fourth-order segments (Figure 3). EA2 and WA4 are the only segments clearly disrupted by smaller discontinuities interpreted as fourth-order discontinuities. The absence of clear fourth-order discontinuities along the other segments does not indicate that only segments EA2 and WA4 are subdivided, instead the complex morphology of the axis does not allow their identification.

Previous studies have often used changes in the VA trend greater than 5° to identified third-order discontinuities of the axis with a limited resolution (Macdonald, 2001; Macdonald et al., 1988). Along the Alarcón Rise, most of the discontinuities are associated with a change in trend smaller than 5° (Table 1). The largest orientation changes are associated with the prolongation of the ridge axis in the transform faults. Changes in the axis trend differ in the northern and southern part of the ridge. Near the Tamayo transform (Figure 2a), the curvature of the ridge is accommodated at the third-order discontinuities, whereas near the Pescadero transform (Figure 2d), WA5 varies gradually by more than 60° over a distance of 10 km to become parallel to the transform without apparent disruption of the axis. Progressive changes in the trend of an undisrupted VA suggests magmatic injection along a curved dike reflecting the progressive change in stress trajectory, whereas the short and discontinuous third-order segments in the southern part of the ridge indicate that the curvature of the ridge is accommodating through smaller intrusions.

Other parameters are known to change at third-order segments, such as volcanic facies, hydrothermal activity, and lava composition (e.g., Carbotte et al., 2015; Macdonald, 2001; Macdonald et al., 1988; White et al., 2000, 2002). White et al. (2002) observed that lava morphology evolves along third-order segments of the EPR (e.g., 18°30′S-17°15′S and 9°08′N-10°N). Channelized flows, which have higher effusion rate, are mainly observed at the center of the segment, whereas hummocky flows, which have lower effusion rate, dominate toward the ends. A similar distribution of flow morphology is observed along EA2, where hummocky flows are the main morphology on EA2a and EA2f and channelized flows predominate from EA2b to EA2e where the ridge is the most inflated. This distribution of volcanic facies also correlates with a variation in the VA geometry (depth and width). From EA2b to EA2e the axis is relatively narrow (<167 m) and corresponds to an eruptive fissure indicating that voluminous and frequent eruptions may have covered older fractures. In contrast, at both ends (EA2a and EA2f) the larger VA (up to 371 m) with more visible fractures indicates a lower magmatic input near the ends of third-order segments. This distribution, is however, not observed along the rest of the ridge and may reveal lower magmatic input at the end of larger-scale segments.

The hydrothermal system is also impacted by fine-scale segmentation. Along WA and EA, the variation is not only marked at the third-order scale but also as fourth order, as predicted by Haymon (1996) and corroborated by other observations along the EPR (e.g., White et al., 2002). Indeed, the presence and the activity of chimneys vary from one fourth-order segment to another corroborating their link to individual magmatic injections. The variation in hydrothermal activity seems directly linked to the focus of the magmatic activity with active vents only located along EA2e and WA3, in the most inflated part of the ridge.

Finally, lava flow composition may vary from one segment to another (Detrick et al., 2002; Langmuir et al., 1986; Sinton et al., 1991; Sinton et al., 2003). It is particularly obvious in the northern part of the Alarcón Rise, where the third-order discontinuity at 23°32.25′N is associated with a dramatic change in lava composition, with basalt south of the discontinuity changing to more evolved compositions to the north (basaltic andesite, andesite, dacite, and rhyolite; Clague et al., 2018).

5.1.2. Endeavour Segmentation

Along the Endeavour Segment, the lack of well-defined eruptive fissures in the AV makes it difficult to precisely locate the current VA and third- and fourth-order discontinuities are not clearly displayed. The center of the AV, halfway between the valley wall, is used as a proxy for the location of the VA. This axis is clearly disrupted by two discontinuities over a distance of 23 km (Figures 5a and 6). These discontinuities associated with lateral offsets of the VA greater than 500 m are consistent with third-order discontinuities described along the EPR (Le Saout et al., 2014; White et al., 2006) or the GSC (Sinton et al., 2003).

The along-axis seafloor depth, measured at the valley rims, does not show bulge shape variation along each AV, but the third-order segment AV2 is shallowest at the segment center and the axis deepens through AV1 and AV3 (Figure 6c). The along-axis depth variation may be the result of the combination of two processes. First, the vestige of the past volcanic activity of the ridge before it rifted. Indeed, during the last high magmatic period, the volcanic activity was mainly focused along AV2, where it built a 300-m-high, 12-km-long, and now 4-km-wide volcanic domed axial high, which during the more recent tectonic and hydrothermal periods (Clague et al., 2014) has become heavily faulted, creating the present-day ~1-km-wide AV. Second, the valley floor is also shallowest within AV2 and deepens through AV1 and AV3. The bulge shape of the valley floor indicates the potential reinflation of the ridge associated with the return of the magmatic

activity as shown by the unfaulted flows, the high density of hydrothermal vents, and the seismicity interpreted as a reinflation of the magma lens and dike intrusion (Weekly et al., 2013; Wilcock et al., 2009).

Third-order segments also become narrower and shallower at their distal ends (Figures 6a and 6b). The presence of overlapping third-order segments, between AV1 and AV2 for example (Figure 5a), could explain their narrower width at their distal ends (Figure 6b) with the extension distributed along two parallel axes instead of only one. However, the cumulative width of the overlapping axes is not wider than the width of the segment at its center. The greater depth of the AV at the overlap and the geometry of the AV do not reflect the accommodation of uniform extension along the axis. It rather indicates that extension is greater in the center of third-order segments, as is volcanic activity.

As along the Alarcón Rise, the discontinuities at the Endeavour Segment are associated with variation in the magmatic and hydrothermal activity within the valley. The young unfaulted flows, only observed along AV2 (Figure 5c), define the recent volcanic activity of the ridge. The hydrothermal vents also vary between each segment (Figure 5d). The discontinuity at 47°55.56′N is associated with a shift in the hydrothermal axis as well as variation in hydrothermal activity, with active fields mainly located in AV2. The discontinuity at 48°1.2′N marks the transition between a hydrothermally active AV2 and an AV3 without hydrothermal chimneys. This observation is consistent with previous studies that noted that third-order segmentation affects hydrothermal activity (Haymon et al., 1991; White et al., 2000).

The hydrothermal axis within AV2 is affected by another shift (210 m toward the east) at 47°58.6′N that is associated with a potential fourth-order discontinuity (between AV2a and AV2b; Figure 5a). South of 47°58.6′N the hydrothermal vents in the Mothra, Main Endeavour Field and High-Rise fields are located along the western base of the AV (AV2a group in Figure 5d), whereas along the north part of the segment, the main hydrothermal activity at Salty Dawg and Sasquatch hydrothermal fields is located along the eastern side of the AV (along AV2b). The change in the hydrothermal axis, hydrothermal circulation, and the discontinuity between the unfractured flows axis indicates a potential fourth-order discontinuity at 47°58.6′N where AV2 is subdivided by a horst. This discontinuity is associated with a 510-m lateral offset. The location of the unfractured flows and the chimneys distribution would indicate that south of 47°58.6′N, the heat and volcanic activity is focused along the west side of the valley, while north of that discontinuity the activity is located along the east side of the valley.

5.2. Preliminary Correlation Between Tectonic and Magmatic Discontinuities

Seismic reflection profiles at the Endeavour Segment imaged multiple disruptions of the axial magma lens (AML; Van Ark et al., 2007). Based on first-order interpretation, Van Ark et al. (2007) defined three disruptions of the magma lens between 47°52.2′N and 48°4.4′N, at ~47°54.7′N, 47°56.8′N, and 48°0.5′N. The two larger disruptions of the AML correspond to gaps of magma lenses over distances exceeding 2 km and are directly linked to the locations of the third-order discontinuities identified in the bathymetry (Figure 6). These third-order discontinuities are also associated with variation in melt content with higher melt content in the center of AV2 evidenced by seismic tomography (Arnoux et al., 2019). The disruption of the magma lens between AV1 and AV2 also marks a transition in the lava composition from normal MORB to transitional and enriched MORB. Similar relations between tectonic and magmatic discontinuities have been documented along the EPR (Carbotte et al., 2000, 2013; Le Saout et al., 2014; White et al., 2000), and third-order tectonic discontinuities have been interpreted to reflect variation in crustal melt volume, which decreases near discontinuities of the magma lens (e.g., Arnoux et al., 2019; Carbotte et al., 2015; White et al., 2000).

A smaller disruption of the AML was imaged beneath AV2 associated with the overlaps of two AML reflectors (Figure 6). There is no discernable tectonic discontinuity above it, nor is the tectonic discontinuity between AV2a and AV2b associated with an imaged disruption in the AML below. As a correlation between magmatic and tectonic fourth-order segmentation has been observed at 9°N on the EPR (Carbotte et al., 2013; Marjanović et al., 2018), the absence of similar correlation along the Endeavour Segment could be due to (1) the lack of well defined volcanic axes that do not allow the precise location of the fourth-order discontinuities and (2) the potential presence of other smaller discontinuities of the AML not yet identified. However, the fourth-order tectonic discontinuity correlates with the northern extent of a region of magmatic injection as inferred by Wilcock et al. (2009) based on the

microearthquake distribution. These observations corroborate the direct relation between fourth-order segmentation and individual magmatic events.

Along the Alarcón Rise, no seismic survey has been collected, and so the presence and disruption of the magma lens can only be estimated based on the morphology of the ridge, the distribution of the tectonic discontinuities, and the variation in lava chemistry. The domed axial high, the volume of high-eruption rate flows produced, and the ages of the flows observed all along the ridge indicate that the segment is in a magmatic phase. Along the EPR (e.g., Carbotte et al., 2013; Marjanović et al., 2018), and the GSC (Sinton et al., 2003), ridges characterized by an axial high also have segmented magma lenses. At the Alarcon Rise, we therefore expect a magma lens to be present along its entire length, or at least under the third-order segment EA2, where the ridge is the most inflated and the youngest and most vigorous volcanic activity occurs (Clague et al., 2018). Based on the observation that third-order segments are often underlain by individual volcanic plumbing systems (White et al., 2000) associated with higher mantle and crustal melt at the segment center (Arnoux et al., 2019), and on the correlations between tectonic and magmatic discontinuities observed along the Endeavour Segment and EPR segments (Carbotte et al., 2013; Han et al., 2014; Le Saout et al., 2014; Marjanović et al., 2018), the magma lens underlying the Alarcón Rise is most likely segmented. Disruptions of the magma lens probably lie beneath each third-order discontinuity along the EA, which is associated with more recent volcanic activity. Another disruption of the AML should be present around 23°30′N where EA yields to WA and the transition in magma composition occurs (Clague et al., 2018). Indeed, this tectonic discontinuity marks the boundary between two distinguishable units erupted over a period of at least 12 kyr: basaltic on the south and basaltic-andesite to rhyolite on the north (Clague et al., 2018). The distinct composition reflects the presence of two different parental magmas (Detrick et al., 2002; Sinton et al., 2003) and indicates two disconnected magmatic origins. Smaller disruptions may also exist beneath fourth-order discontinuities as revealed in high-resolution seismic data along 9°N segments (Carbotte et al., 2013, Marjanović et al., 2018).

5.3. Evolution of Third-Order Segments at Intermediate Ridges

The evolution of fine-scale segmentation is often hard to evaluate since third- and fourth-order discontinuities rarely leave off-axis traces (Macdonald et al., 1992; White et al., 2000). Their longevity is not clearly known, but some are estimated to persist for 100 kyr (e.g., Carbotte et al., 2015). Both the Alarcón Rise and the Endeavour Segment do not provide enough evidence of the fine-scale segmentation variation over periods of 100 kyr, but they offer opportunities to look at their variations over periods of 300 to 4,300 years.

5.3.1. Evolution During High Magmatic Phase

Along the Alarcón Rise, several parameters reflect a shift of the VA toward the east during at least the last 300 years. At different locations along the ridge axis, the eastern wall of the WA graben is partially erased and WA fissures and channel systems partially filled by lava flows erupted along EA (Figure 2a), and forming the broad dome across EA (Figure 1b, profile (1) suggesting that EA marks the most recent volcanic activity. This observation is corroborated by relative sediment thickness and by ^{14}C ages of the base layer of those sediments that reveal ages between 80 year and 33.8 kyr for flows erupted along WA and ages younger than 300 years for flows erupted along EA (Figures 2c and 3d; Clague et al., 2018). Where comparison of deformation induced by dike intrusions between the two axes is possible (Figure 4), the higher extension rate along EA indicates that this axis has accommodated more deformation and thus probably experienced more dike intrusions.

The eastward migration is most pronounced in the southern part of the ridge (e.g., the 1,300 m offset between WA2 and EA2 vs. 85 m between WA4 and EA3) and has not affected the ridge north of EA3 (Figure 2d). This may be a result of the recent volcanic activity being focused along EA2 and/or a south to north progression of the axis shift. The migration could also be influenced by a 3° counterclockwise rotation of the axis, which could be an accommodation of the opening of the Gulf of California. The reorientation of the ridge axis would slightly realign the Alarcón Rise (~N32°E) toward the orientation of the other spreading basins of the gulf (e.g., ~N7°E for the southern Pescadero Basin).

Over the last 300 years the eruptive axis has not only migrated laterally, but some fine-scale discontinuities also may have migrated along the axis. The presence of similar discontinuities between eastern and western axes, around 23°16.5′N (between WA1 and WA2, and EA1 and EA2) and at 23°27.2′N (between WA4a and

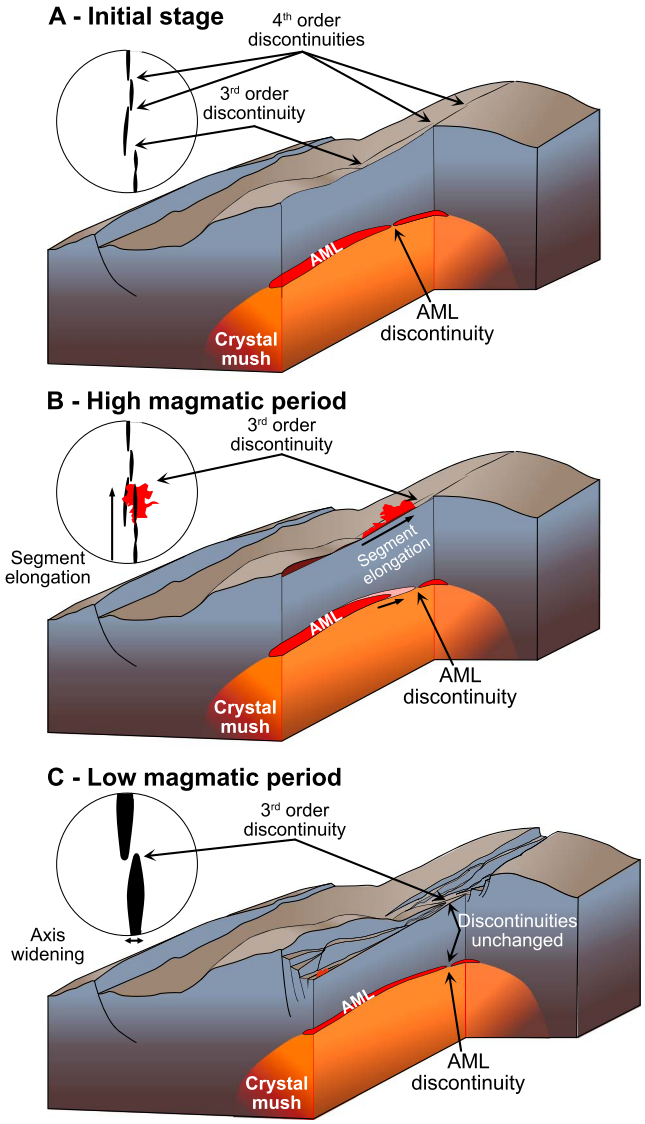

Figure 7. Illustration of the evolution of fine-scale segmentation at intermediate-spreading ridges during a hypothetical progression through high and low magmatic periods. The circle insets represent the top view of each 3-D block at the same scale. Recent flows are shown in red and the axis segments are marked by black bold lines. (a) Initial stage: the ridge is disrupted by third- and fourth-order discontinuities. The third-order discontinuity is associated with a disruption of the axial magma lens (AML). (b) High magmatic period is associated with rapid evolution of third-order segments that propagate through multiple eruptions. This propagation may be associated by an elongation of the AML. (c) During low magmatic periods, the axes widen but the locations of the third-order discontinuities remain unchanged and fourth-order discontinuities are erased.

WA4b, and EA2 to EA3), indicates that lateral migration of the volcanic activity does not affect the segmentation of the ridge, and older axis segmentation can be used as a marker of the evolution of the segmentation. The migration of the discontinuities along the axis is clearly seen in the southern part of the ridge where it is associated with an elongation of 8 km of EA2 compared to WA3, a regression of 7.7 km of EA3 compared to WA4, and the disappearance of WA2. EA3 regression is associated with low volcanic activity that is indicated by the presence of few pillow mounds. Similar evolution is known to occur along second-order segments (Carbotte & Macdonald, 1992; Cormier & Macdonald, 1994; Klein et al., 2013). They are associated with variation of the magmatic activity, and they propagate due to elongation of "warm" segments at the expense of "cold" segments (Thibaud et al., 1998). Along the Alarcón Rise, the difference between WA and EA may be attributed to a similar process because the segment that elongates is located in the most inflated part of the ridge as well as the place characterized by the youngest and most effusive flows. Thus, during the last 300 years, EA2 experienced a lengthening at a mean speed of about 26 m/year. This corroborates that third-order segments tend to evolve in the same way as second order segments, with the lengthening of "warm" segments (Figure 7b) at least during intense magmatic phases (Le Saout et al., 2014; Thibaud et al., 1998).

5.3.2. Evolution During Low Magmatic Phase

At the Endeavour Segment, the third-order segmentation is estimated using disruptions that shaped the valley walls. The absence of asymmetry in the cross-axis morphology (Figure 1, profile 2) and flow direction on both sides of the axis indicates that the extension had occurred along the VA. The discontinuity of the valley wall would thus reflect the position of the VA at the end of the last magmatic phase more than 4,300 years ago (Clague et al., 2014).

There is no morphological evidence, such as the presence of eruptive fissures or volcanic ridge, to determine the current third-order segmentation with precision. However, the correlation between the hydrothermal vents distribution and the magma lens discontinuities is a good proxy to estimate the current third-order segmentation. Except at 47°57.4′N where a slight change in the magma lens is observed, all current discontinuities coincide with the discontinuities of the VA when the high magmatic phase ended 4,300 years ago. The only evidence, the migration of a third order discontinuities during the last 4,300 years, is the extension toward the north by 1.5 km of AV2b compared to AV2a (Figures 5 and 6). This would indicate a focus of the magmatic activity along AV2b with an average propagation of 0.35 m/year over the last 4,300 years. However, the propagation probably occurs during the recent increase of magmatic activity. This indicates that during low magmatic periods, third-order segmentation of the VA, and of the underlying magma chamber do not vary significantly (Figure 7c). Fourth-order discontinuities that are not preserved may vary even during low magmatic periods due to small eruptive events.

5.4. Comparison Between Intermediate- and Fast-Spreading Ridge Segmentation

Fine-scale segmentation along intermediate-spreading axes presents similar characteristics to what is observed along fast-spreading ridges. Along the Alarcón Rise and the Endeavour Segment the third-order segments are 4.5 to 23.5 km long and the fourth-order segments are 0.4 to 9.1 km long (Table 3). Their

Table 3
Comparison of the Fine-Scale Segmentation With Previous Studies at Fast- and Intermediate-Spreading Ridges

	Intermediate-spreading ridges		Fast-spreading ridges		
	Alarcón	Endeavour	EPR-16N[a]	EPR-9N[b]	
Generality					
Spreading rate (mm/year)	52	56/52	85	110	
Morphology	axial high	axial valley	axial high	axial high	
Northern and southern boundaries	2 transforms	2 OSC	1 transform + 1 OSC	1 transform + 1 OSC	
Number of hydrothermal vents	175 (57 actives)	767 (21 actives)	22 (2 actives)	36 sites actives	
Axis jump	yes	no	yes	no	
Hot spot interaction	no	yes	yes	no	
Along axis length of the study area (km)	51	23	32	55	133
Discontinuity					
Number of 3rd order discontinuities	2 (4)	2	5	3	4
Number of 4rd order discontinuities	5 (3)	1	5	7	10
Third-order segment length (km)	11-26.3	14.7	4-10	31/38	15/38
Fourth-order segment length (km)	0.4-9.1	7.2-7.5	1.1-4.5	3.9/12.4	3.9/12.9
Number of AML discontinuities	No Data	3[c]	6	10	18
Axis morphology					
AST general morphology	no AST/fissures/graben	wide graben	narrow wide AST	no AST/narrow/wide AST	
AST width (m)	0-600	150-1400	8-1100	no 50/320	
AST depth (m)	0-33	5-110	0.5-40	1-20	
Parallel and synchronous axes	yes	no	yes	no	

Abbreviations: AML, axial magma lens; AST, axial summit trough.
[a]Values from Le Saout et al. (2014) and Carbotte et al. (2000). [b]Values from Soule et al. (2009) and White et al. (2000, 2002). [c]Number of disruption of the axial magma lens (AML) from Van Ark et al. (2007).

dimensions are in the same range of segments measured along the EPR with 4-38 km long for third-order segments and 1.1-12.9 km long for fourth-order segments at 9 and 16°N along the EPR (e.g., Le Saout et al., 2014; Soule et al., 2009; White et al., 2000, 2002). Third-order segments appear directly related to the underlying magma lenses and evolved over at least hundreds to thousands of years. This evolution stagnates during low magmatic phases at intermediate-spreading ridges but may evolve relatively rapidly during robust magmatic activity. Similar to the EPR, third-order segments seem disrupted into shorter fourth-order segments marked by changes in hydrothermal chimney distribution and in the main volcanic facies. These observations corroborate previous studies along the EPR suggesting that third-order segmentation affects the entire crustal system. The relation between tectonic and magmatic disruption is, however, not always reflected in fourth-order discontinuities.

6. Conclusion

Our high-resolution bathymetric analysis of the Alarcón Rise and the Endeavour Segment axes provides information on the fine-scale segmentation of intermediate ridges and the evolution of this segmentation through the tectono-magmatic cycle. In both segments, the VA is disrupted by up to 950-m offsets that mark transitions in the axis, flow morphology, hydrothermal activity, and in lava flow compositions. The geometry of the segments and associated offsets is similar in morphology and dimension to those described along the fast-spreading EPR. Fine-scale discontinuities at intermediate-spreading ridges, as at fast spreading ridges, are divided into third-order and fourth order discontinuities. Third-order appears associated with disruptions of the underlying magma lens as revealed by seismic reflection and tomography, whereas fourth-order discontinuities mark the transitions between individual magmatic events and influence hydrothermal chimney distribution. With the available data, no correlation between AML and tectonic discontinuity at the fourth-order scale has been identified along the two intermediate-spreading ridges.

The Alarcón Rise and the Endeavour Segment show past and current fine-scale segmentation of the axis. At the Alarcón Rise, a recent and progressive transition of volcanic activity toward the east has resulted in the presence of two volcanic axes with distinct fine-scale segmentation. At the Endeavour Segment, past segmentation is revealed by the disruption and geometry of the axial graben walls, whereas the recent segmentation is indicated by the distribution of hydrothermal vents, young flows, and disruptions of the underlying

magma lens. The comparison between old and current axes shows that the evolution of the fine-scale segmentation (third- and fourth-order) varies depending on magmatic activity. During high magmatic periods, segments evolve rapidly, with lengthening of the most active third-order segment that can elongate at a mean rate of 26 m/year. In periods of low magmatic activity, dominated by tectonic deformation and/or hydrothermal activity, segmentation remains at a relatively steady state or is affected by only slight changes.

Acknowledgments
Processed AUV bathymetry is available at the IEDA Marine Geoscience Data System repository. For the Alarcón Rise, the DOI is 10.1594/IEDA/324366. For the Endeavour Segment, DOIs are 10.1594/IEDA/321996 and 10.1594/IEDA/321973. Technical figures describing the methods are in the supporting information. We thank the captains and crew members of the multiple expeditions that collected the data combined in this paper as well as the AUV teams without whom this work would not have been possible. We thank E. Hooft, M. Marjanović, and an anonymous reviewer for their constructive comments that greatly improved this manuscript. This work was part of a postdoctoral fellowship at MBARI founded by the David and Lucile Packard Foundation.

References

Arnoux, G. M., Toomey, D. R., Hooft, E. E. E., & Wilcock, W. S. D. (2019). Seismic imaging and physical properties of the Endeavour segment: Evidence that skew between mantle and crustal magmatic systems governs spreading center processes. *Geochemistry, Geophysics, Geosystems*, *20*, 1319–1339. https://doi.org/10.1029/2018GC007978

Bhat, V., Shaw, P. R., & Delaney, J. R. (1997). The Endeavour Ridge as observed by DSL120 sidescan sonar: Interplay of volcanic, tectonic, and hydrothermal processes. *Eos, Transactions American Geophysical Union*, *78*, 46.

Buck, W. R., & Poliakov, A. N. B. (1998). Abyssal hills formed by stretching oceanic lithosphere. *Nature*, *392*(6673), 272–275. https://doi.org/10.1038/32636

Carbotte, S. M., Detrick, R. S., Harding, A., Canales, J. P., Babcock, J., Kent, G., et al. (2006). Rift topography linked to magmatism at the intermediate spreading Juan de Fuca Ridge. *Geology*, *34*(3), 209–212. https://doi.org/10.1130/G21969.1

Carbotte, S. M., & Macdonald, K. (1992). East Pacific Rise 8–10 30′ N: Evolution of ridge segments and discontinuities from SeaMARC II and three-dimensional magnetic studies. *Journal of Geophysical Research*, *97*(B5), 6959–6982. https://doi.org/10.1029/91JB03065

Carbotte, S. M., Marjanović, M., Carton, H., Mutter, J. C., Canales, J. P., Nedimović, M. R., et al. (2013). Fine-scale segmentation of the crustal magma reservoir beneath the East Pacific Rise. *Nature Geoscience*, *6*(10), 866–870. https://doi.org/10.1038/ngeo1933

Carbotte, S. M., Small, C., & Donnelly, K. (2004). The influence of ridge migration on the magmatic segmentation of mid-ocean ridges. *Nature*, *429*(6993), 743–746. https://doi.org/10.1038/nature02652

Carbotte, S. M., Smith, D. K., Cannat, M., & Klein, E. M. (2015). Tectonic and magmatic segmentation of the Global Ocean Ridge System: A synthesis of observations. *Geological Society, London, Special Publications*, *420*, SP420–SP425.

Carbotte, S. M., Solomon, A., & Ponce-Correa, G. (2000). Evaluation of morphological indicators of magma supply and segmentation from a seismic reflection study of the East Pacific Rise 15°30′–17°N. *Journal of Geophysical Research*, *105*(B2), 2737–2759. https://doi.org/10.1029/1999JB900245

Caress, D. W., Troni, G., Clague, D. A., Paduan, J. B., Martin, J. F., Thomas, H. J., et al. (2015). Detection of active hydrothermal vent fields in the Pescadero Basin and on the Alarcon Rise using AUV multibeam and CTD data. Abstract OS23C-2027 presented at the American Geophysical Union Fall Meeting, San Francisco, December 14-18.

Chadwick, W. W., & Embley, R. W. (1998). Graben formation associated with recent dike intrusions and volcanic eruptions on the mid-ocean ridge. *Journal of Geophysical Research*, *103*(B5), 9807–9825. https://doi.org/10.1029/97JB02485

Christie, D. M., Werner, R., Hauff, F., Hoernle, K., & Hanan, B. B. (2005). Morphological and geochemical variations along the eastern Galápagos Spreading Center. *Geochemistry, Geophysics, Geosystems*, *6*, Q01006. https://doi.org/10.1029/2004GC000714

Clague, D. A., Dreyer, B. M., Paduan, J. B., Martin, J. F., Caress, D. W., Gill, J. B., et al. (2014). Eruptive and tectonic history of the Endeavour Segment, Juan de Fuca Ridge, based on AUV mapping data and lava flow ages. *Geochemistry, Geophysics, Geosystems*, *15*, 3364–3391. https://doi.org/10.1002/2014GC005415

Clague, D. A., Paduan, J. B., Caress, D. W., Chadwick, W. W. Jr., Le Saout, M., Dreyer, B. M., & Portner, R. A. (2017). High-resolution AUV mapping and targeted ROV observations of three historical lava flows at Axial Seamount. *Oceanography*, *30*(4). https://doi.org/10.5670/oceanog.2017.426

Clague, D. A., Caress, D. W., Dreyer, B. M., Lundsten, L., Paduan, J. B., Portner, R. A., et al. (2018). Geology of the Alarcon Rise, Southern Gulf of California. *Geochemistry, Geophysics, Geosystems*, *19*, 807–837. https://doi.org/10.1002/2017GC007348

Cormier, M.-H., & Macdonald, K. C. (1994). East Pacific Rise 18–19 S: Asymmetric spreading and ridge reorientation by ultrafast migration of axial discontinuities. *Journal of Geophysical Research*, *99*(B1), 543–564. https://doi.org/10.1029/93JB02382

Cormier, M.-H., Ryan, W. B. F., Shah, A. K., Jin, W., Bradley, A. M., & Yoerger, D. R. (2003). Waxing and waning volcanism along the East Pacific Rise on a millennium time scale. *Geology*, *31*(7), 633–636. https://doi.org/10.1130/0091-7613(2003)031<0633:WAWVAT>2.0.CO;2

Cousens, B. L., Allan, J. F., Leybourne, M. I., Chase, R. L., & Van Wagoner, N. (1995). Mixing of magmas from enriched and depleted mantle sources in the northeast Pacific: West Valley segment, Juan de Fuca Ridge. *Contributions to Mineralogy and Petrology*, *120*(3–4), 337–357. https://doi.org/10.1007/BF00306512

Delaney, J. R., Kelley, D. S., Lilley, M. D., Butterfield, D. A., McDuff, R. E., & Baross, J. A. (1997). Temporal/spatial exploration of physical, chemical, and biological linkages in a submarine hydrothermal laboratory: The Endeavour Ridge. *Eos, Transactions American Geophysical Union*, *78*, 46.

Delaney, J. R., Robigou, V., McDuff, R. E., & Tivey, M. K. (1992). Geology of a vigorous hydrothermal system on the Endeavour Segment, Juan de Fuca Ridge. *Journal of Geophysical Research*, *97*(B13), 19,663–19,682. https://doi.org/10.1029/92JB00174

DeMets, C., Gordon, R. G., & Argus, D. F. (2010). Geologically current plate motions. *Geophysical Journal International*, *181*(1), 1–80. https://doi.org/10.1111/j.1365-246X.2009.04491.x

Detrick, R. S., Sinton, J. M., Ito, G., Canales, J. P., Behn, M., Blacic, T., et al. (2002). Correlated geophysical, geochemical, and volcanological manifestations of plume-ridge interaction along the Galápagos Spreading Center. *Geochemistry, Geophysics, Geosystems*, *3*(10), 8501. https://doi.org/10.1029/2002GC000350

Gente, P., Pockalny, R. A., Durand, C., Deplus, C., Maia, M., Ceuleneer, G., et al. (1995). Characteristics and evolution of the segmentation of the Mid-Atlantic Ridge between 20 N and 24 N during the last 10 million years. *Earth and Planetary Science Letters*, *129*(1–4), 55–71. https://doi.org/10.1016/0012-821X(94)00233-O

Gill, J., Michael, P., Woodcock, J., Dreyer, B., Ramos, F., Clague, D., et al. (2016). Spatial and Temporal Scale of Mantle Enrichment at the Endeavour Segment, Juan de Fuca Ridge. *Journal of Petrology*, *57*(5), 863–896. https://doi.org/10.1093/petrology/egw024

Gill, J., Michael, P., Woodcock, J., Dreyer, B., Ramos, F., Clague, D., et al. (2018). Corrigendum to: 'Spatial and temporal scale of mantle enrichment at the Endeavour Segment, Juan de Fuca Ridge'. *Journal of Petrology*, *59*(9), 1845–1845. https://doi.org/10.1093/petrology/egy076

Glickson, D. A., Kelley, D. S., & Delaney, J. R. (2007). Geology and hydrothermal evolution of the Mothra hydrothermal field, Endeavour Segment, Juan de Fuca Ridge. *Geochemistry, Geophysics, Geosystems*, *8*, Q06010. https://doi.org/10.1029/2007GC001588

Han, S., Carbotte, S. M., Carton, H., Mutter, J. C., Aghaei, O., Nedimović, M. R., & Canales, J. P. (2014). Architecture of on-and off-axis magma bodies at EPR 9°37–40′N and implications for oceanic crustal accretion. *Earth and Planetary Science Letters*, *390*, 31–44. https://doi.org/10.1016/j.epsl.2013.12.040

Haymon, R. M. (1996). The response of ridge-crest hydrothermal systems to segmented, episodic magma supply. *Geological Society, London, Special Publications*, *118*(1), 157–168. https://doi.org/10.1144/GSL.SP.1996.118.01.09

Haymon, R. M., Fornari, D. J., Edwards, M. H., Carbotte, S. M., Wright, D., & MacDonald, K. C. (1991). Hydrothermal vent distribution along the East Pacific Rise crest (9°09′-54′N) and its relationship to magmatic and tectonic processes on fast-spreading mid-ocean ridges. *Earth and Planetary Science Letters*, *104*(2–4), 513–534. https://doi.org/10.1016/0012-821X(91)90226-8

Haymon, R. M., & White, S. M. (2004). Fine scale segmentation of volcanic/hydrothermal systems along fast-spreading ridge crests. *Earth and Planetary Science Letters*, *226*(3–4), 367–382. https://doi.org/10.1016/j.epsl.2004.08.002

Hey, R., Baker, E., Bohnenstiehl, D., Massoth, G., Kleinrock, M., Martinez, F., et al. (2004). Tectonic/volcanic segmentation and controls on hydrothermal venting along Earth's fastest seafloor spreading system, EPR 27–32 S. *Geochemistry, Geophysics, Geosystems*, *5*, Q12007. https://doi.org/10.1029/2004GC000764

Jamieson, J. W., Clague, D. A., & Hannington, M. D. (2014). Hydrothermal sulfide accumulation along the Endeavour segment, Juan de Fuca Ridge. *Earth and Planetary Science Letters*, *395*, 136–148. https://doi.org/10.1016/j.epsl.2014.03.035

Jamieson, J. W., Hannington, M. D., Clague, D. A., Kelley, D. S., Delaney, J. R., Holden, J. F., et al. (2013). Sulfide geochronology along the Endeavour Segment of the Juan de Fuca Ridge. *Geochemistry, Geophysics, Geosystems*, *14*, 2084–2099. https://doi.org/10.1002/ggge.20133

Kappel, E. S., & Ryan, W. B. F. (1986). Volcanic episodicity and a non-steady state rift valley along Northeast Pacific spreading centers: Evidence from Sea MARC I. *Journal of Geophysical Research*, *91*(B14), 13925. https://doi.org/10.1029/JB091iB14p13925

Karsten, J. L., Delaney, J. R., Rhodes, J. M., & Liias, R. A. (1990). Spatial and temporal evolution of magmatic systems beneath the Endeavour Segment, Juan de Fuca Ridge: Tectonic and petrologic constraints. *Journal of Geophysical Research*, *95*(B12), 19,235–19,256. https://doi.org/10.1029/JB095iB12p19235

Karsten, J. L., Hammond, S. R., Davis, E. E., & Currie, R. G. (1986). Detailed geomorphology and neotectonics of the Endeavour Segment, Juan de Fuca Ridge: New results from Seabeam swath mapping. *Geological Society of America Bulletin*, *97*(2), 213–221. https://doi.org/10.1130/0016-7606(1986)97<213:DGANOT>2.0.CO;2

Kelley, D. S., Carbotte, S. M., Caress, D. W., Clague, D. A., Delaney, J. R., Gill, J. B., et al. (2012). Endeavour Segment of the Juan de Fuca Ridge: One of the most remarkable places on Earth. *Oceanography*, *25*(1), 44–61. https://doi.org/10.5670/oceanog.2012.03

Kelley, D. S., Karson, J. A., Blackman, D. K., FruÈh-Green, G. L., Butterfield, D. A., Lilley, M. D., et al. (2001). An off-axis hydrothermal vent field near the Mid-Atlantic Ridge at 30 N. *Nature*, *412*(6843), 145–149. https://doi.org/10.1038/35084000

Klein, E. M., White, S. M., Nunnery, J. A., Mason-Stack, J. L., Wanless, V. D., Perfit, M. R., et al. (2013). Seafloor photo-geology and sonar terrain modeling at the 9°N overlapping spreading center, East Pacific Rise. *Geochemistry, Geophysics, Geosystems*, *14*, 5146–5170. https://doi.org/10.1002/2013GC004858

Langmuir, C. H., Bender, J. F., & Batiza, R. (1986). Petrological and tectonic segmentation of the East Pacific Rise, 5 30'-14 30'N. *Nature*, *322*(6078), 422–429. https://doi.org/10.1038/322422a0

Le Saout, M., Deschamps, A., Soule, S. A., & Gente, P. (2014). Segmentation and eruptive activity along the East Pacific Rise at 16 N, in relation with the nearby Mathematician hotspot. *Geochemistry, Geophysics, Geosystems*, *15*, 4380–4399. https://doi.org/10.1002/2014GC005560

Le Saout, M., Thibaud, R., & Gente, P. (2018). Detailed analysis of near tectonic features along the East Pacific Rise at 16°N, near the Mathematician Hot Spot. *Journal of Geophysical Research: Solid Earth*, *123*, 4478–4499. https://doi.org/10.1029/2017JB015301

Lewis, B. T. (1979). Periodicities in volcanism and longitudinal magma flow on the East Pacific Rise at 23 N. *Geophysical Research Letters*, *6*(10), 753–756. https://doi.org/10.1029/GL006i010p00753

Lilley, M. D., Feely, R. A., & Trefry, J. H. (1995). Chemical and biochemical transformations in hydrothermal plumes. In S. E. Humphris, R. A. Zierenberg, L. S. Mullineaux, & R. E. Thomson (Eds.), *Seafloor hydrothermal systems: Physical, chemical, biological, and geological interactions*, *Geophysical Monograph Series*, (Vol. 91, pp. 369–391). Washington, DC: American Geophysical Union.

Lizarralde, D., Axen, G. J., Brown, H. E., Fletcher, J. M., Gonzales-Fernandez, A., Harding, A. J., et al. (2007). Variations in styles of rifting in the Gulf of California. *Nature*, *448*(7152), 466–469. https://doi.org/10.1038/nature06035

Lonsdale, P. (1994). Structural geomorphology of the Eltanin fault system and adjacent transform faults of the Pacific-Antarctic plate boundary. *Marine Geophysical Researches*, *16*(2), 105–143. https://doi.org/10.1007/BF01224756

Macdonald, K. C. (2001). Mid-ocean ridge tectonics, volcanism, and geomorphology. In J. H. Steele, K. K. Turekian, & S. A. Thorpe (Eds.), *Encyclopedia of Ocean Sciences*, (pp. 852–866). Oxford: Academic Press.

Macdonald, K. C., Fox, P. J., Miller, S., Carbotte, S., Edwards, M. H., Eisen, M., et al. (1992). The East Pacific Rise and its flanks 8–18 N: History of segmentation, propagation and spreading direction based on SeaMARC II and Sea Beam studies. *Marine Geophysical Researches*, *14*(4), 299–344. https://doi.org/10.1007/BF01203621

Macdonald, K. C., Fox, P. J., Perram, L. J., Eisen, M. F., Haymon, R. M., Miller, S. P., et al. (1988). A new view of the mid-ocean ridge from the behaviour of ridge-axis discontinuities. *Nature*, *335*(6187), 217–225. https://doi.org/10.1038/335217a0

Malinverno, A., & Pockalny, R. A. (1990). Abyssal hill topography as an indicator of episodicity in crustal accretion and deformation. *Earth and Planetary Science Letters*, *99*(1-2), 154–169. https://doi.org/10.1016/0012-821X(90)90079-D

Marjanović, M., Carbotte, S. M., Carton, H., Nedimović, M. R., Canales, J. P., & Mutter, J. C. (2018). Crustal magmatic system beneath the East Pacific Rise (8°20′ to 10°10′N): Implications for tectono-magmatic segmentation and melt transport at fast-spreading ridges. *Geochemistry, Geophysics, Geosystems*, *19*, 4584–4611. https://doi.org/10.1029/2018GC007590

Paduan, J. B., Zierenberg, R., Clague, D. A., Spelz, R. M., Caress, D. W., Troni, G., et al. (2018). Discovery of hydrothermal vent fields on Alarcón Rise and in Southern Pescadero Basin, Gulf of California. *Geochemistry, Geophysics, Geosystems*, *19*, 4788–4819. https://doi.org/10.1029/2018GC007771

Pezard, P. A., Anderson, R. N., Ryan, W. B., Becker, K., Alt, J. C., & Gente, P. (1992). Accretion, structure and hydrology of intermediate spreading-rate oceanic crust from drillhole experiments and seafloor observations. *Marine Geophysical Researches*, *14*(2), 93–123. https://doi.org/10.1007/BF01204282

Poliakov, A. N., & Buck, W. R. (1998). Mechanics of stretching elastic-plastic-viscous layers: Applications to slow-spreading mid-ocean ridges. In W. R. Buck, P. T. Delaney, J. A. Karson, & Y. Lagabrielle (Eds.), *Faulting and magmatism at mid-ocean ridges*, *Geophysical Monograph Series*, (Vol. 106, pp. 305–323). Washington, DC: American Geophysical Union.

Robigou, V., Delaney, J. R., & Stakes, D. S. (1993). Large massive sulfide deposits in a newly discovered active hydrothermal system, the High-Rise field, Endeavour segment, Juan de Fuca Ridge. *Geophysical Research Letters*, *20*(17), 1887–1890. https://doi.org/10.1029/93GL01399

Sempéré, J.-C., Lin, J., Brown, H. S., Schouten, H., & Purdy, G. M. (1993). Segmentation and morphotectonic variations along a slow-spreading center: The Mid-Atlantic Ridge (24 00′ N–30 40′ N). *Marine Geophysical Researches*, *15*(3), 153–200. https://doi.org/10.1007/BF01204232

Sempéré, J.-C., Purdy, G. M., & Schouten, H. (1990). Segmentation of the Mid-Atlantic Ridge between 24 N and 30 40'N. *Nature*, *344*(6265), 427–431. https://doi.org/10.1038/344427a0

Shoberg, T., Stein, S., & Karsten, J. (1991). Constraints on rift propagation history at the Cobb Offset, Juan de Fuca Ridge, from numerical modeling of tectonic fabric. *Tectonophysics*, *197*(2–4), 295–308. https://doi.org/10.1016/0040-1951(91)90047-V

Sinton, J. M., Detrick, R., Canales, J. P., Ito, G., & Behn, M. (2003). Morphology and segmentation of the western Galápagos Spreading Center, 90.5°–98°W: Plume-ridge interaction at an intermediate spreading ridge. *Geochemistry, Geophysics, Geosystems*, *4*(12), 8515. https://doi.org/10.1029/2003GC000609

Sinton, J. M., Smaglik, S. M., Mahoney, J. J., & Macdonald, K. C. (1991). Magmatic processes at superfast spreading mid-ocean ridges: Glass compositional variations along the East Pacific Rise 13–23 S. *Journal of Geophysical Research*, *96*(B4), 6133–6155. https://doi.org/10.1029/90JB02454

Soule, S. A., Escartin, J., & Fornari, D. J. (2009). A record of eruption and intrusion at a fast spreading ridge axis; axial summit trough of the East Pacific Rise at 9-10 degrees N. *Geochemistry, Geophysics, Geosystems*, *10*, Q10T07. https://doi.org/10.1029/2008GC002354

Sutherland, F. H. (2006). Continental rifting across the southern Gulf of California (Doctoral dissertation). San Diego, CA: University of California.

Szitkar, F., Dyment, J., Le Saout, M., Honsho, C., & Gente, P. (2016). Dyking at EPR 16° N hypermagmatic ridge segment: Insights from near-seafloor magnetics. *Earth and Planetary Science Letters*, *453*, 288–297. https://doi.org/10.1016/j.epsl.2016.08.020

Thibaud, R., Gente, P., & Maia, M. (1998). A systematic analysis of the Mid-Atlantic Ridge morphology and gravity between 15 N and 40 N: Constraints of the thermal structure. *Journal of Geophysical Research*, *103*(B10), 24,223–24,243. https://doi.org/10.1029/97JB02934

Tivey, M. K., & Delaney, J. R. (1986). Growth of large sulfide structures on the endeavour segment of the Juan de Fuca ridge. *Earth and Planetary Science Letters*, *77*(3-4), 303–317. https://doi.org/10.1016/0012-821X(86)90142-1

Toomey, D. R., Jousselin, D., Dunn, R. A., Wilcock, W. S. D., & Detrick, R. S. (2007). Skew of mantle upwelling beneath the East Pacific Rise governs segmentation. *Nature*, *446*(7134), 409–414. https://doi.org/10.1038/nature05679

Van Ark, E. M., Detrick, R. S., Canales, J. P., Carbotte, S. M., Harding, A. J., Kent, G. M., et al. (2007). Seismic structure of the Endeavour Segment, Juan de Fuca Ridge: Correlations with seismicity and hydrothermal activity. *Journal of Geophysical Research*, *112*, B02401. https://doi.org/10.1029/2005JB004210

VanderBeek, B. P., Toomey, D. R., Hooft, E. E., & Wilcock, W. S. (2016). Segmentation of mid-ocean ridges attributed to oblique mantle divergence. *Nature Geoscience*, *9*(8), 636–642. https://doi.org/10.1038/NGEO2745

Weekly, R. T., Wilcock, W. S. D., Hooft, E. E. E., Toomey, D. R., McGill, P. R., & Stakes, D. S. (2013). Termination of a 6 year ridge-spreading event observed using a seafloor seismic network on the Endeavour Segment, Juan de Fuca Ridge. *Geochemistry, Geophysics, Geosystems*, *14*, 1375–1398. https://doi.org/10.1002/ggge.20105

White, S. M., Haymon, R. M., & Carbotte, S. (2006). A new view of ridge segmentation and near-axis volcanism at the East Pacific Rise, 8°–12°N, from EM300 multibeam bathymetry. *Geochemistry, Geophysics, Geosystems*, *7*, Q12O05. https://doi.org/10.1029/2006GC001407

White, S. M., Haymon, R. M., Fornari, D. J., Perfit, M. R., & Macdonald, K. C. (2002). Correlation between volcanic and tectonic segmentation of fast-spreading ridges; evidence from volcanic structures and laval flow morphology on the East Pacific Rise at 9°-10°N. *Journal of Geophysical Research*, *107*(B8), 2173. https://doi.org/10.1029/2001JB000571

White, S. M., Macdonald, K. C., & Haymon, R. M. (2000). Basaltic lava domes, lava lakes, and volcanic segmentation on the southern East Pacific Rise. *Journal of Geophysical Research*, *105*(B10), 23,519–23,536. https://doi.org/10.1029/2000JB900248

White, S. M., Meyer, J. D., Haymon, R. M., Macdonald, K. C., Baker, E. T., & Resing, J. A. (2008). High-resolution surveys along the hot spot–affected Galápagos Spreading Center: 2. Influence of magma supply on volcanic morphology. *Geochemistry, Geophysics, Geosystems*, *9*, Q09004. https://doi.org/10.1029/2008GC002036

Wilcock, W. S., Hooft, E. E., Toomey, D. R., McGill, P. R., Barclay, A. H., Stakes, D. S., & Ramirez, T. M. (2009). The role of magma injection in localizing black-smoker activity. *Nature Geoscience*, *2*(7), 509–513. https://doi.org/10.1038/ngeo550

Wilson, D. S. (1993). Confidence intervals for motion and deformation of the Juan de Fuca plate. *Journal of Geophysical Research*, *98*(B9), 16053–16071. https://doi.org/10.1029/93JB01227